

# STATE SPACE GEOMETRY OF A SPATIO-TEMPORALLY CHAOTIC KURAMOTO-SIVASHINSKY FLOW



PREDRAG CVITANOVIĆ\*, RUSLAN L. DAVIDCHACK† AND EVANGELOS SIMINOS\*

**Abstract.** The continuous and discrete symmetries of the Kuramoto-Sivashinsky system restricted to a spatially periodic domain play a prominent role in shaping the invariant sets of its spatiotemporally chaotic dynamics. The continuous spatial translation symmetry leads to relative equilibria (traveling wave) and relative periodic orbit solutions. The discrete symmetries lead to existence of equilibrium and periodic orbit solutions, induce decomposition of state space into orthogonal invariant subspaces, and enforce certain structurally stable heteroclinic connections between equilibria. We show, on example of a particular small-cell Kuramoto-Sivashinsky system, how the geometry of its dynamical state space is organized by a rigid ‘cage’ built by heteroclinic connections between equilibria, and demonstrate the preponderance of unstable relative periodic orbits and their likely role as the skeleton underpinning spatiotemporal turbulence in systems with continuous symmetries. We also offer novel visualizations of the high-dimensional Kuramoto-Sivashinsky state space flow through projections onto low-dimensional, PDE representation independent, dynamically invariant intrinsic coordinate frames, as well as in terms of the physical, symmetry invariant energy transfer rates.

**Key words.** relative periodic orbits, chaos, turbulence, continuous symmetry, Kuramoto-Sivashinsky equation

**AMS subject classifications.** 35B05, 35B10, 37L05, 37L20, 76F20, 65H10, 90C53

**1. Introduction.** Recent experimental and theoretical advances [15] support a dynamical vision of turbulence: For any finite spatial resolution, a turbulent flow follows approximately for a finite time a pattern belonging to a finite alphabet of admissible patterns. The long term dynamics is a walk through the space of these unstable patterns. The question is how to characterize and classify such patterns? Here we follow the seminal Hopf paper [17], and visualize turbulence not as a sequence of spatial snapshots in turbulent evolution, but as a trajectory in an  $\infty$ - $d$  state space in which an instant in turbulent evolution is a unique point. In the dynamical systems approach, theory of turbulence for a given system, with given boundary conditions, is given by the (a) geometry of the state space and (b) the associated natural measure, that is, the likelihood that asymptotic dynamics visits a given state space region.

We pursue this program in context of the Kuramoto-Sivashinsky (KS) equation, one of the simplest physically interesting spatially extended nonlinear systems. Holmes, Lumley and Berkooz [16] offer a delightful discussion of why this system deserves study as a staging ground for studying turbulence in full-fledged Navier-Stokes boundary shear flows.

Dynamical state space representation of a PDE is  $\infty$ -dimensional, but the KS flow is strongly contracting and its non-wondering set, and, within it, the set of invariant solutions investigated here, is embedded into a finite-dimensional inertial manifold [9] in a non-trivial, nonlinear way. ‘Geometry’ in the title of this paper refers to our attempt to systematically triangulate this set in terms of dynamically invariant solutions (equilibria, periodic orbits, ...) and their unstable manifolds, in a PDE representation and numerical simulation algorithm independent way. The goal is to describe a given ‘turbulent’ flow quantitatively, not model it qualitatively by a low-dimensional model. For the case investigated here, the state space representation

---

\*School of Physics, Georgia Institute of Technology, Atlanta, GA 30332-0430, USA

†Department of Mathematics, University of Leicester, University Road, Leicester LE1 7RH, UK

dimension  $d \sim 10^2$  is set by requiring that the exact invariant solutions that we compute are accurate to  $\sim 10^{-5}$ . The state space is high-dimensional, the asymptotic dynamics is confined to a low-dimensional subspace, so we are in the gray, ill-defined overlapping zone between ‘turbulence’ and ‘spatiotemporal chaos,’ the two terms that we shall use interchangeably in what follows.

In previous work, the state space geometry and the natural measure for this system have been studied [3, 22, 23] in terms of unstable periodic solutions restricted to the antisymmetric subspace of the KS dynamics.

The focus in this paper is on the role continuous symmetries play in spatiotemporal dynamics. The notion of exact periodicity in time is replaced by the notion of relative spatiotemporal periodicity, and relative equilibria and relative periodic orbits here play the role the equilibria and periodic orbits played in the earlier studies. Our search for relative periodic orbits in KS system was inspired by Vanessa López [24] investigation of relative periodic orbits of the Complex Ginzburg-Landau equation. However, there is a vast literature on relative periodic orbits since their first appearance, in Poincaré study of the 3-body problem [2, 28], where the Lagrange points are the relative equilibria. They arise in dynamics of systems with continuous symmetries, such as motions of rigid bodies, gravitational  $N$ -body problems, molecules and nonlinear waves. Very recently Viswanath [29] has found both relative equilibria and relative periodic orbits in the plane Couette problem.

Building upon the pioneering work of refs. [20, 14], we undertake here a study of the Kuramoto-Sivashinsky dynamics for a specific system size  $L = 22$ , sufficiently large to exhibit many of the features typical of ‘turbulent’ dynamics observed in large KS systems, but small enough to lend itself to a detailed exploration of the equilibria and relative equilibria, their stable/unstable manifolds, determination of a large number of relative periodic orbits, and a preliminary exploration of the relation between the observed spatiotemporal ‘turbulent’ patterns and the relative periodic orbits.

In presence of a continuous symmetry any solution belongs to a group manifold of equivalent solutions. The problem: If one is to generalize the periodic orbit theory to this setting, one needs to understand what is meant by solutions being nearby (shadowing) when each solution belongs to a manifold of equivalent solutions. We resolve here this puzzle by demonstrating that if one picks any particular solution, the universe of all other solutions is rigidly fixed through a web of heteroclinic connections between them. This insight garnered from study of a 1-dimensional Kuramoto-Sivashinsky PDE is more remarkable still when applied to the plane Couette flow [13], with 3- $d$  velocity fields and two translational symmetries.

The main results presented here are: (a) Dynamics visualized through physical, symmetry invariant observables, such as ‘energy,’ dissipation rate, *etc.*, and through projections onto dynamically invariant, PDE-discretization independent state space coordinate frames, sect. 3. (b) Existence of a rigid ‘cage’ built by heteroclinic connections between equilibria, sect. 4. (c) Preponderance of unstable relative periodic orbits and their likely role as the skeleton underpinning spatiotemporal turbulence in systems with continuous symmetries, sect. 6.

**2. Kuramoto-Sivashinsky equation.** The Kuramoto-Sivashinsky [henceforth KS] system [21, 27], which arises in the description of stability of flame fronts, reaction-diffusion systems and many other physical settings [20], is one of the simplest nonlinear PDEs that exhibit spatiotemporally chaotic behavior. In the formulation adopted here, the time evolution of the ‘flame front velocity’  $u = u(x, t)$  on a periodic domain

$u(x, t) = u(x + L, t)$  is given by

$$u_t = F(u) = -\frac{1}{2}(u^2)_x - u_{xx} - u_{xxx}, \quad x \in [-L/2, L/2]. \quad (2.1)$$


Here  $t \geq 0$  is the time, and  $x$  is the spatial coordinate. The subscripts  $x$  and  $t$  denote partial derivatives with respect to  $x$  and  $t$ . In what follows we shall state results of all calculations either in units of the ‘dimensionless system size’  $\tilde{L}$ , or the system size  $L = 2\pi\tilde{L}$ . Figure 2.1 presents a typical ‘turbulent’ evolution for KS. All numerical results presented in this paper are for the system size  $\tilde{L} = 22/2\pi = 3.5014\dots$ . Spatial periodicity  $u(x, t) = u(x + L, t)$  makes it convenient to work in the Fourier space,

$$u(x, t) = \sum_{k=-\infty}^{+\infty} a_k(t) e^{ikx/\tilde{L}}, \quad (2.2)$$

with the 1-dimensional PDE (2.1) replaced by an infinite set of ODEs for the complex Fourier coefficients  $a_k(t)$ :

$$\dot{a}_k = v_k(a) = (q_k^2 - q_k^4) a_k - i \frac{q_k}{2} \sum_{m=-\infty}^{+\infty} a_m a_{k-m}, \quad (2.3)$$

where  $q_k = k/\tilde{L}$ . Since  $u(x, t)$  is real,  $a_k = a_{-k}^*$ , and we can replace the sum by a  $k > 0$  sum.

Due to the hyperviscous damping  $u_{xxx}$ , long time solutions of KS equation are smooth,  $a_k$  drop off fast with  $k$ , and truncations of (2.3) to  $16 \leq N \leq 128$  terms yield accurate solutions for system sizes considered here (see Appendix A). Robustness of the long-time dynamics of KS as a function of the number of Fourier modes kept in truncations of (2.3) is, however, a subtle issue. Adding an extra mode to a truncation of the system introduces a small perturbation in the space of dynamical systems. However, due to the lack of structural stability both as a function of truncation  $N$ , and the system size  $\tilde{L}$ , a small variation in a system parameter can (and often will) throw the dynamics into a different asymptotic state. For example, asymptotic attractor which appears to be chaotic in a  $N$ -dimensional state space truncation can collapse into an attractive cycle for  $(N+1)$ -dimensions. 

**2.1. Symmetries of Kuramoto-Sivashinsky equation.** The KS equation is Galilean invariant: if  $u(x, t)$  is a solution, then  $u(x - ct, t) - c$ , with  $c$  an arbitrary constant speed, is also a solution. Without loss of generality, in our calculations we shall set the mean velocity of the front to zero,

$$\int dx u = 0. \quad (2.4)$$

As  $\dot{a}_0 = 0$  in (2.3),  $a_0$  is a conserved quantity fixed to  $a_0 = 0$  by the condition (2.4).  $G$ , the group of actions  $g \in G$  on a state space (reflections, translations, etc.) is a symmetry of the KS flow (2.1) if  $g u_t = F(g u)$ . The KS equation is time translationally invariant, and space translationally invariant on a periodic domain under the 1-parameter group of  $O(2) : \{\tau_{\ell/L}, R\}$ . If  $u(x, t)$  is a solution, then  $\tau_{\ell/L} u(x, t) = u(x + \ell, t)$  is an equivalent solution for any shift  $-L/2 < \ell \leq L/2$ , as is the reflection (‘parity’ or ‘inversion’)

$$R u(x) = -u(-x). \quad (2.5)$$

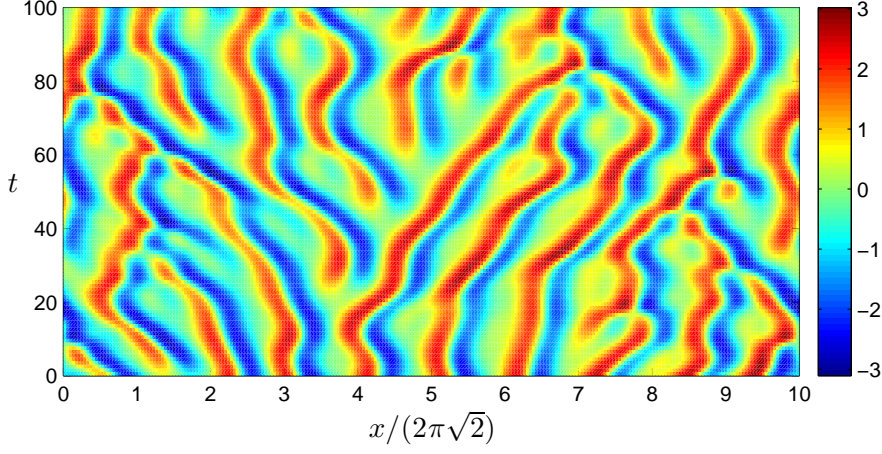


FIG. 2.1. A typical ‘turbulent’ solution of the Kuramoto-Sivashinsky equation, system size  $L = 20\pi\sqrt{2} \approx 88.86$ . The  $x$  coordinate is scaled with the most unstable wavelength  $2\pi\sqrt{2}$ , which is approximately also the mean wavelength of the turbulent flow. The color bar indicates the color scheme for  $u(x, t)$ , used also for the subsequent figures of this type.

The translation operator action on the Fourier coefficients (2.2), represented here by a complex valued vector  $a = \{a_k \in \mathbb{C} \mid k = 1, 2, \dots\}$ , is given by

$$\tau_{\ell/L} a = \mathbf{g}(\ell) a, \quad (2.6)$$

where  $\mathbf{g}(\ell) = \text{diag}(e^{iq_k \ell})$  is a complex valued diagonal matrix, which amounts to the  $k$ -th mode complex plane rotation by an angle  $k\ell/\tilde{L}$ . The reflection acts on the Fourier coefficients by complex conjugation,

$$Ra = -a^*. \quad (2.7)$$

Reflection generates the dihedral subgroup  $D_1 = \{1, R\}$  of  $O(2)$ . Let  $\mathbb{U}$  be the space of real-valued velocity fields periodic and square integrable on the interval  $\Omega = [-L/2, L/2]$ ,

$$\mathbb{U} = \{u \in L^2(\Omega) \mid u(x) = u(x + L)\}. \quad (2.8)$$

A continuous symmetry maps each state  $u \in \mathbb{U}$  to a manifold of functions with identical dynamic behavior. Relation  $R^2 = 1$  induces linear decomposition  $u(x) = u^+(x) + u^-(x)$ ,  $u^\pm(x) = P^\pm u(x) \in \mathbb{U}^\pm$ , into irreducible subspaces  $\mathbb{U} = \mathbb{U}^+ \oplus \mathbb{U}^-$ , where

$$P^+ = (1 + R)/2, \quad P^- = (1 - R)/2, \quad (2.9)$$

are the antisymmetric/symmetric projection operators. Applying  $P^+$ ,  $P^-$  on the KS equation (2.1) we have [20]

$$\begin{aligned} u_t^+ &= -(u^+ u_x^+ + u^- u_x^-) - u_{xx}^+ - u_{xxxx}^+ \\ u_t^- &= -(u^+ u_x^- + u^- u_x^+) - u_{xx}^- - u_{xxxx}^-. \end{aligned} \quad (2.10)$$

If  $u^- = 0$ , KS flow is confined to the antisymmetric  $\mathbb{U}^+$  subspace,

$$u_t^+ = -u^+ u_x^+ - u_{xx}^+ - u_{xxxx}^+, \quad (2.11)$$

but otherwise the nonlinear terms in (2.10) mix the two subspaces.

Together with any rational shift  $\tau_{1/m}u(x) = u(x + L/m)$  reflection generates a discrete dihedral subgroup  $D_m$  of  $O(2)$ , also a symmetry of KS system. The only non-zero Fourier components of a solution invariant under  $D_m$  are  $a_{jm} \neq 0$ ,  $j = 1, 2, \dots$ .  $D_m$  reduces the dimensionality of state space and aids computation of equilibria and periodic orbits within it. For example, the 1/2-cell translations

$$\tau_{1/2} u(x) = u(x + L/2) \quad (2.12)$$

and reflections generate  $O(2)$  subgroup  $D_2 = \{1, R, \tau, \tau R\}$ , which reduces the state space into four irreducible subspaces (for brevity, here  $\tau = \tau_{1/2}$ ):

$$\begin{array}{ccccc} & & \tau & R & \tau R \\ P^{(1)} = \frac{1}{4}(1 + \tau + R + \tau R) & S & S & S \\ P^{(2)} = \frac{1}{4}(1 + \tau - R - \tau R) & S & A & A \\ P^{(3)} = \frac{1}{4}(1 - \tau + R - \tau R) & A & S & A \\ P^{(4)} = \frac{1}{4}(1 - \tau - R + \tau R) & A & A & S. \end{array} \quad (2.13)$$

$P^{(j)}$  is the projection operator onto  $u^{(j)}$  irreducible subspace, and the last 3 columns refer to the symmetry (or antisymmetry) of  $u^{(j)}$  functions under reflection and 1/2-cell shift. By the same argument that identified (2.11) as the invariant subspace of KS, here the KS flow stays within the  $\mathbb{U}^S = \mathbb{U}^{(1)} + \mathbb{U}^{(2)}$  irreducible  $D_1$  subspace of  $u$  profiles symmetric under 1/2-cell shifts.

While in general the bilinear term  $(u^2)_x$  mixes the irreducible subspaces of  $D_n$ , for  $D_2$  there are four subspaces invariant under the flow [20]:

$\{0\}$ : the  $u(x) = 0$  equilibrium

$\mathbb{U}^+ = \mathbb{U}^{(1)} + \mathbb{U}^{(3)}$ : the reflection  $D_1$  irreducible space of antisymmetric  $u(x)$

$\mathbb{U}^S = \mathbb{U}^{(1)} + \mathbb{U}^{(2)}$ : the shift  $D_1$  irreducible space of  $L/2$  shift symmetric  $u(x)$

$\mathbb{U}^{(1)}$ : the  $D_2$  irreducible space of  $u(x)$  invariant under  $x \mapsto L/2 - x$ ,  $u \mapsto -u$ .

With the continuous translational symmetry eliminated within each subspace, there are no relative equilibria and relative periodic orbits, and one can focus on the equilibria and periodic orbits only, as was done for  $\mathbb{U}^+$  in refs. [3, 22, 23]. In the Fourier representation, the  $u \in \mathbb{U}^+$  antisymmetry amounts to having purely imaginary coefficients, since  $a_{-k} = a_k^* = -a_k$ . The 1/2 cell-size shift  $\tau_{1/2}$  generated 2-element discrete subgroup  $\{1, \tau_{1/2}\}$  is of particular interest because in the  $\mathbb{U}^+$  subspace the translational invariance of the full system reduces to invariance under discrete translation (2.12) by half a spatial period  $L/2$ .

Each of the above dynamically invariant subspaces is unstable under small perturbations, and generic solutions of Kuramoto-Sivashinsky equation belong to the full space. Nevertheless, since all equilibria of the KS flow studied in this paper lie in the  $\mathbb{U}^+$  subspace (see sect. 4),  $\mathbb{U}^+$  plays important role for the global geometry of the flow. However, linear stability of these equilibria has eigenvectors both in and outside of  $\mathbb{U}^+$ , and needs to be computed in the full state space.

**2.2. Equilibria and relative equilibria.** Equilibria (or the steady solutions) are the fixed profile time-invariant solutions,

$$u(x, t) = u_q(x). \quad (2.14)$$

Due to the translational symmetry, the KS system also allows for relative equilibria (traveling waves, rotating waves), characterized by a fixed profile  $u_q(x)$  moving with constant speed  $c$ , that is

$$u(x, t) = u_q(x - ct). \quad (2.15)$$

Here suffix  $_q$  labels a particular invariant solution. Because of the reflection symmetry (2.5), the relative equilibria come in counter-traveling pairs  $u_q(x - ct)$ ,  $-u_q(-x + ct)$ .

The relative equilibrium condition for the Kuramoto-Sivashinsky PDE (2.1) is the ODE

$$\frac{1}{2}(u^2)_x + u_{xx} + u_{xxxx} = cu_x \quad (2.16)$$

which can be analyzed as a dynamical system in its own right. Integrating once we get

$$\frac{1}{2}u^2 - cu + u_x + u_{xxx} = E. \quad (2.17)$$

This equation can be interpreted as a 3-dimensional dynamical system with spatial coordinate  $x$  playing the role of ‘time,’ and the integration constant  $E$  can be interpreted as ‘energy,’ see sect. 3.

For  $E > 0$  there is rich  $E$ -dependent dynamics, with fractal sets of bounded solutions investigated in depth by Michelson [25]. For  $\tilde{L} < 1$  the only equilibrium of the system is the globally attracting constant solution  $u(x, t) = 0$ , denoted  $E_0$  from now on. With increasing system size  $L$  the system undergoes a series of bifurcations. The resulting equilibria and relative equilibria (but not periodic orbits and relative periodic orbits) are described in the classical papers of Kevrekidis, Nicolaenko and Scovel [20], and Greene and Kim [14]. The relevant bifurcations up to the system size investigated here are summarized in Figure 2.2: at  $\tilde{L} = 22/2\pi = 3.5014 \dots$ , the equilibria are the constant solution  $E_0$ , the GLMRT [26, 14] equilibrium  $E_1$ , the 2- and 3-cell states  $E_2$  and  $E_3$ , and the pairs of relative equilibria  $TW_{\pm 1}$ ,  $TW_{\pm 2}$ .

In the Fourier representation the relative equilibria time dependence is

$$a_k(t)e^{-itcq_k} = a_k(0). \quad (2.18)$$

Differentiating with respect to time, we obtain the Fourier space version of the relative equilibrium condition (2.16),

$$v_k(a) - iq_kca_k = 0, \quad (2.19)$$

which we solve for (time independent)  $a_k$  and  $c$ . Periods of spatially periodic equilibria are multiples of  $L$ . Every time the system size crosses  $\tilde{L} = n$ ,  $n$ -cell states are generated through pitchfork bifurcations off  $u = 0$  equilibrium. Due to the translational invariance of Kuramoto-Sivashinsky equation, they form invariant circles in the full state space. In the  $\mathbb{U}^+$  subspace considered here, they correspond to  $2n$  points, each shifted by  $L/2n$ . For a sufficiently small  $L$  the number of equilibria is small and concentrated on the low wave-number end of the Fourier spectrum.

In a periodic box of size  $L$  both equilibria and relative equilibria are periodic solutions embedded in 3- $d$  space, conveniently represented as loops in  $(u, u_x, u_{xx})$  space, see Figure 5.1 (d). In this representation the continuous translation symmetry is automatic – a rotation in the  $[0, L]$  periodic domain only moves the points along the loop. For an equilibrium the points are stationary in time; for relative equilibrium

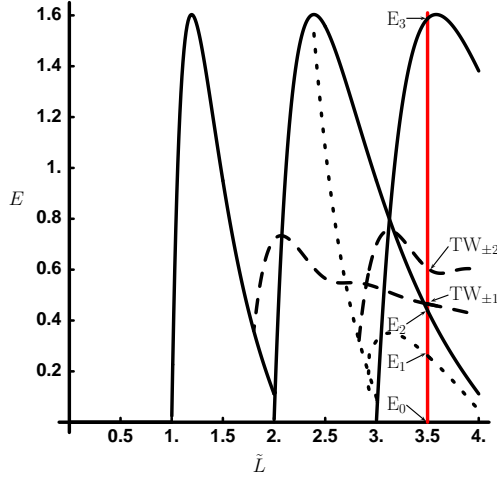


FIG. 2.2. The energy (3.6) of the equilibria and relative equilibria that exist up to  $L = 22$ ,  $\tilde{L} = 3.5014\dots$ , plotted as a function of the system size  $\tilde{L} = L/2\pi$  (additional equilibria, not present at  $L = 22$  are given in ref. [14]). Solid curves denote  $n$ -cell solutions  $E_2$  and  $E_3$ , dotted curves the GLMRT equilibrium  $E_1$ , and dashed curves the relative equilibria  $TW_{\pm 1}$  and  $TW_{\pm 2}$ . The parameter  $\alpha$  of refs. [20, 14] is related to the system size by  $\tilde{L} = \sqrt{\alpha/4}$ .

they move in time, but in either case, the loop remains invariant. So we do not have the problem that we encounter in the Fourier representation, where seen from the frame of one of the equilibria the rest trace out circles under the action of continuous symmetry translations.

From (2.3) we see that the origin  $u(x, t) = 0$  has Fourier modes as the linear stability eigenvectors (see Appendix B). The  $|k| < \tilde{L}$  long wavelength perturbations of the flat-front equilibrium are linearly unstable, while all  $|k| > \tilde{L}$  short wavelength perturbations are strongly contractive. The high  $k$  eigenvalues, corresponding to rapid variations of the flame front, decay so fast that the corresponding eigendirections are physically irrelevant. The most unstable mode, nearest to  $|k| = \tilde{L}/\sqrt{2}$ , sets the scale of the mean wavelength  $\sqrt{2}$  of the KS ‘turbulent’ dynamics, see Figure 2.1.

**2.3. Relative periodic orbits, symmetries and periodic orbits.** The KS equation (2.1) is time translationally invariant, and space translationally invariant under the 1- $d$  Lie group of  $O(2)$  rotations: if  $u(x, t)$  is a solution, then  $u(x + \ell, t)$  and  $-u(-x, t)$  are equivalent solutions for any  $-L/2 < \ell \leq L/2$ . As a result of invariance under  $\tau_{\ell/L}$ , KS equation can have relative periodic orbit solutions with a profile  $u_p(x)$ , period  $T_p$ , and a nonzero shift  $\ell_p$

$$\tau_{\ell_p/L} u(x, T_p) = u(x + \ell_p, T_p) = u(x, 0) = u_p(x). \quad (2.20)$$

Due to invariance under reflections, KS equation can have pre-periodic solution characterized by a profile  $u_p(x)$ , period  $T_p$

$$Ru(x + \ell, T_p) = -u(-x - \ell, T_p) = u(x + \ell, 0) = u_p(x), \quad (2.21)$$

the family of equivalent solutions parameterized by  $\ell$  (as the choice of the reflection point is arbitrary, the shift can take any value in  $-L/2 < \ell \leq L/2$ ). Relative periodic orbits (2.20) are periodic in  $v_p = \ell_p/T_p$  co-rotating frame (see Figure 8.3), but in the



stationary frame their trajectories are quasiperiodic. Due to the reflection symmetry (2.5) of KS equation, every relative periodic orbit  $u_p(x)$  with shift  $\ell_p$  has a symmetric partner  $-u_p(-x)$  with shift  $-\ell_p$ .

As  $\ell$  is continuous in the interval  $[-L/2, L/2]$ , the likelihood of a relative periodic orbit with  $\ell_p = 0$  shift is zero, unless an exact periodicity is enforced by a discrete symmetry, such as the dihedral symmetries discussed above. If the shift  $\ell_p$  of a relative periodic orbit with period  $T_p$  is such that  $\ell_p/L$  is a rational number, then the orbit is periodic with period  $nT_p$ . The likelihood to find such periodic orbits is also zero.

However, due to the KS equation invariance under reflection (2.5), two types of periodic orbits are possible:

(a) The periodic orbit lies within the  $\mathbb{U}^+$  antisymmetric subspace,  $-u_p(-x) = u_p(x)$ , and  $u(x, T_p) = u(x, 0) = u_p(x)$ .

(b) If an orbit is of reflection type (2.21),  $R\tau_{\ell/L}u(x, T_p) = -u(-x - \ell, T_p) = u(x, 0)$ , then it is pre-periodic to a periodic orbit with period  $2T_p$ . Indeed, since  $(R\tau_{\ell/L})^2 = R^2 = 1$ , and the KS solutions are time translation invariant, it follows from (2.21) that

$$u(x, 2T_p) = R\tau_{\ell/L}u(x, T_p) = (R\tau_{\ell/L})^2u(x, 0) = u(x, 0) .$$

Thus any shift acquired during time 0 to  $T_p$  is compensated by the opposite shift during evolution from  $T_p$  to  $2T_p$ . Such pre-periodic orbits are a hallmark of any dynamical system with a discrete symmetry, where they have a natural interpretation as periodic orbits in the fundamental domain [8, 7].

**3. Energy transfer rates.** In physical settings where the observation times are much longer than the dynamical ‘turnover’ and Lyapunov times (statistical mechanics, quantum physics, turbulence) periodic orbit theory [7] provides highly accurate predictions of measurable long-time averages such as the dissipation and the turbulent drag [13]. Physical predictions have to be independent of a particular choice of ODE representation of the PDE under consideration and, most importantly, invariant under all symmetries of the dynamics. In this section we discuss a set of such physical observables for the 1- $d$  KS invariant under reflections and translations. They offer a representation of dynamics in which the symmetries are explicitly quotiented out. We shall use these observable in sect. 8 in order to visualize a set of solutions on these coordinates.

The space average of a function  $a = a(x, t) = a(u(x, t))$  on the interval  $L$ ,

$$\langle a \rangle = \frac{1}{L} \oint dx \, a(x, t) , \quad (3.1)$$

is in general time dependent. Its mean value is given by the time average

$$\bar{a} = \lim_{t \rightarrow \infty} \frac{1}{t} \int_0^t d\tau \, \langle a \rangle = \lim_{t \rightarrow \infty} \frac{1}{t} \int_0^t \frac{1}{L} \oint d\tau \, dx \, a(x, \tau) . \quad (3.2)$$

The mean value of  $a = a(u_q) \equiv a_q$  evaluated on  $q$  equilibrium or relative equilibrium  $u(x, t) = u_q(x - ct)$  is

$$\bar{a}_q = \langle a \rangle_q = a_q . \quad (3.3)$$

Evaluation of the infinite time average (3.2) on a function of a periodic orbit or relative periodic orbit  $u_p(x, t) = u_p(x, t + T_p)$  requires only a single  $T_p$  traversal,

$$\bar{a}_p = \frac{1}{T_p} \int_0^{T_p} d\tau \, \langle a \rangle . \quad (3.4)$$



Equation (2.1) can be written as

$$u_t = -V_x, \quad V(x, t) = \frac{1}{2}u^2 + u_x + u_{xxx}. \quad (3.5)$$

If  $u$  is ‘flame-front velocity’ then  $E$ , defined in (2.17), can be interpreted as the mean energy density. So, even though KS is a phenomenological small-amplitude equation, the time-dependent quantity

$$E = \frac{1}{L} \oint dx V(x, t) = \frac{1}{L} \oint dx \frac{u^2}{2} \quad (3.6)$$

has a physical interpretation [14] as the average ‘energy’ density of the flame front. This analogy to the mean kinetic energy density for the Navier-Stokes motivates what follows.

The energy (3.6) is intrinsic to the flow, independent of the particular ODE basis set chosen to represent the PDE. However, as the Fourier amplitudes are eigenvectors of the translation operator, in the Fourier space the energy is a diagonalized quadratic norm,

$$E = \sum_{k=-\infty}^{\infty} E_k, \quad E_k = \frac{1}{2}|a_k|^2, \quad (3.7)$$

and explicitly invariant term by term under translations (2.6) and reflections (2.5).

Take time derivative of the energy density (3.6), substitute (2.1) and integrate by parts. Total derivatives vanish by the spatial periodicity on the  $L$  domain:

$$\begin{aligned} \dot{E} &= \langle u_t u \rangle = - \langle (u^2/2 + u u_x + u u_{xxx})_x u \rangle \\ &= \langle u_x u^2/2 + u_x^2 + u_x u_{xxx} \rangle. \end{aligned} \quad (3.8)$$

The first term in (3.8) vanishes by integration by parts,  $3 \langle u_x u^2 \rangle = \langle (u^3)_x \rangle = 0$ , and integrating the third term by parts yet again one gets [14] that the energy variation

$$\dot{E} = P - D, \quad P = \langle u_x^2 \rangle, \quad D = \langle u_{xx}^2 \rangle \quad (3.9)$$

balances the power  $P$  pumped in by anti-diffusion  $u_{xx}$  against the energy dissipation rate  $D$  by hyper-viscosity  $u_{xxxx}$  in the KS equation (2.1).

The time averaged energy density  $\overline{E}$  computed on a typical orbit goes to a constant, so the expectation values (3.10) of drive and dissipation exactly balance each out:

$$\overline{\dot{E}} = \lim_{t \rightarrow \infty} \frac{1}{t} \int_0^t d\tau \dot{E} = \overline{P} - \overline{D} = 0. \quad (3.10)$$

In particular, the equilibria and relative equilibria fall onto the diagonal in Figure 8.1, and so do time averages computed on periodic orbits and relative periodic orbits:

$$\overline{E}_p = \frac{1}{T_p} \int_0^{T_p} d\tau E(\tau), \quad \overline{P}_p = \frac{1}{T_p} \int_0^{T_p} d\tau P(\tau) = \overline{D}_p. \quad (3.11)$$

In the Fourier basis (3.7) the conservation of energy on average takes form

$$0 = \sum_{k=-\infty}^{\infty} (q_k^2 - q_k^4) \overline{E}_k, \quad E_k(t) = \frac{1}{2}|a_k(t)|^2. \quad (3.12)$$

The large  $k$  convergence of this series is insensitive to the system size  $L$ ;  $\overline{E_k}$  have to decrease much faster than  $q_k^{-4}$ . Deviation of  $E_k$  from this bound for small  $k$  determines the active modes. For equilibria the  $L$ -independent bound on  $E$  is given by Michaelson [25]. The best current bound [12, 1] on the long-time limit of  $E$  as a function of the system size  $L$  scales as  $E \propto L^{3/2}$ .

**4. Geometry of state space with  $L = 22$ .** We now turn to exploring Hopf's vision numerically, on a specific Kuramoto-Sivashinsky system. An instructive example is offered by the dynamics for the  $L = 22$  system that we specialize to for the rest of this paper. The size of this small system is  $\sim 2.5$  mean wavelengths ( $\tilde{L}/\sqrt{2} = 2.4758 \dots$ ), and the competition between states with wavenumbers 2 and 3 leads to the empirically observed 'sustained turbulence.' Asymptotic attractor structure of small systems like the one studied here is very sensitive to system parameter variations, and, as is true of any realistic unsteady flow, there is no rigorous way of establishing that this 'turbulence' is sustained for all time, rather than being merely a very long transient on a way to an attracting periodic state. For large system size, as the one shown in Figure 2.1, it is hard to imagine a scenario under which attractive periodic states (as shown in ref. [11], they do exist) would have significantly large immediate basins of attraction. Regardless of the (non)existence of a  $t \rightarrow \infty$  chaotic attractor, study of the invariant unstable solutions and the associated Smale horseshoe structures in system's state space offers valuable insights into the observed unstable 'coherent structures.'

Because of the strong  $k^4$  contraction, for a small system size one expects that the long-time dynamics is confined to low-dimensional center manifold. Indeed, numerically the leading Lyapunov exponents of the  $L = 22$  chaotic attractor are  $(\lambda_i) = (0.048, 0, 0, -0.003, -0.189, -0.256, -0.290, \dots)$ , so the chaotic dynamics mostly takes place close to a 4-dimensional manifold, with strong contraction in other dimensions. The two zero exponents are due to the time and space translational symmetries of the Kuramoto-Sivashinsky equation, and it was shown in refs. [3, 23] that within particular curvilinear coordinate frames, the dynamics on the attractor can sometimes be reduced to local 1- or 2-dimensional maps. Hence a relatively small number of Fourier modes, typically 128 used in numerical calculations presented here, suffices to obtain numerically accurate (within  $10^{-5}$ ) invariant solutions.

We next investigate the properties of equilibria and relative equilibria and determine numerically a large set of the short periods relative periodic orbits for KS in a periodic cell of size  $L = 22$ .

**5. Equilibria and relative equilibria for  $L = 22$ .** In addition to the trivial equilibrium  $u = 0$  (denoted  $E_0$ ), we find three equilibria with dominant wavenumber  $k$  (denoted  $E_k$ ) for  $k = 1, 2, 3$ . All equilibria, shown in Fig. 5.1, are symmetric with respect to the reflection symmetry (2.5). In addition,  $E_2$  and  $E_3$  are symmetric with respect to translation (2.12), by  $L/2$  and  $L/3$ , respectively.  $E_2$  and  $E_3$  essentially lie, respectively, in the 2<sup>nd</sup> and 3<sup>rd</sup> Fourier component complex plane, with small  $k = 2j$ ,  $k = 3j$  harmonics deformations.

The stability of the equilibria is characterized by the eigenvalues  $\lambda_j$  of the stability matrix. The leading 10 eigenvalues for each equilibrium are listed in Table 5.1. We have computed (available upon request) the corresponding eigenvectors as well. As an equilibrium with  $\text{Re } \lambda_j > 0$  is unstable in the direction of the corresponding eigenvector  $\mathbf{e}^{(j)}$ , the eigenvectors provide flow-intrinsic (PDE discretization independent) coordinates which we use for visualization of unstable manifolds and homo/heteroclinic connections between equilibria.

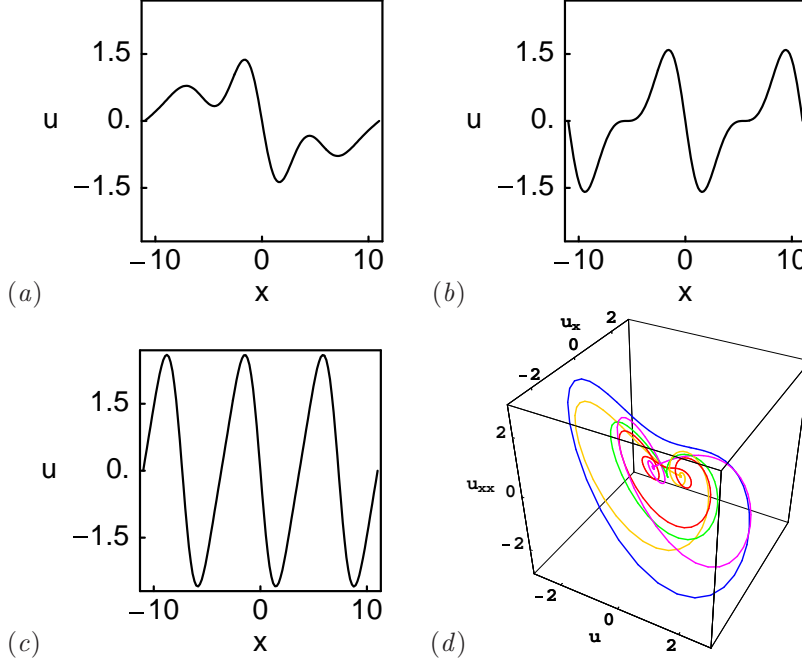


FIG. 5.1. (a)  $E_1$ , (b)  $E_2$ , and (c)  $E_3$  equilibria. The  $E_0$  equilibrium is the  $u(x) = 0$  solution. (d)  $(u, u_x, u_{xx})$  representation of (red)  $E_1$ , (green)  $E_2$ , (blue)  $E_3$  equilibria, (purple)  $TW_{+1}$ , and (orange)  $TW_{-1}$  relative equilibria.  $L = 22$  system size.

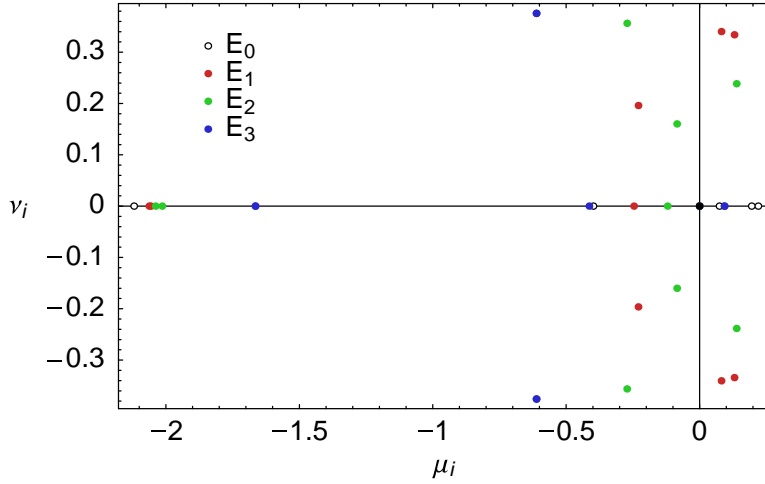


FIG. 5.2. Leading equilibrium stability eigenvalues,  $L = 22$  system size.

The eigenvalues of  $E_0$  are determined by the linear part of the KS equation (B.4):  $\lambda_k = (k/\tilde{L})^2 - (k/\tilde{L})^4$ . For  $L = 22$ , there are three pairs of unstable eigenvalues, corresponding, in decreasing order, to three unstable modes  $k = 2, 3$ , and 1. For each mode, the corresponding eigenvectors lie in the plane spanned by  $\text{Re } a_k$  and  $\text{Im } a_k$ . Table 5.1 lists the symmetries of the stability eigenvectors of equilibria  $E_1$  to  $E_3$ .

Consistent with the bifurcation diagram of Figure 2.2, we find two pairs of relative

TABLE 5.1

Leading eigenvalues  $\lambda_j = \mu_j \pm i\nu_j$  and symmetries of the corresponding eigenvectors of KS equilibria and relative equilibria for  $L = 22$  system size. We have used as our reference states the ones that lie within the antisymmetric subspace  $\mathbb{U}^+$ , and also listed the symmetries of the  $L/4$  translated ones.

$E_1$	$\mu_j$	$\nu_j$	Symmetry	$\tau_{1/4}E_n$ Symmetry
$\lambda_{1,2}$	0.1308	0.3341	-	-
$\lambda_{3,4}$	0.0824	0.3402	$\mathbb{U}^+$	$\mathbb{U}^{(1)}$
$\lambda_5$	0		-	-
$\lambda_{6,7}$	-0.2287	0.1963	$\mathbb{U}^+$	$\mathbb{U}^{(1)}$
$\lambda_8$	-0.2455		-	-
$\lambda_9$	-2.0554		$\mathbb{U}^+$	$\mathbb{U}^{(1)}$
$\lambda_{10}$	-2.0619		-	-
<hr/>				
$E_2$				
$\lambda_{1,2}$	0.1390	0.2384	$\mathbb{U}^+$	$\mathbb{U}^{(1)}$
$\lambda_3$	0		$\tau_{1/2}$	$\tau_{1/2}$
$\lambda_{4,5}$	-0.0840	0.1602	$\mathbb{U}^{(1)}$	$\mathbb{U}^+$
$\lambda_6$	-0.1194		$\tau_{1/2}$	$\tau_{1/2}$
$\lambda_{7,8}$	-0.2711	0.3563	$\mathbb{U}^+, \mathbb{U}^{(1)}, \tau_{1/2}$	$\mathbb{U}^+, \mathbb{U}^{(1)}, \tau_{1/2}$
$\lambda_9$	-2.0130		$\mathbb{U}^{(1)}$	$\mathbb{U}^+$
$\lambda_{10}$	-2.0378		$\mathbb{U}^+$	$\mathbb{U}^{(1)}$
<hr/>				
$E_3$				
$\lambda_1$	0.0933		$\mathbb{U}^+$	$\mathbb{U}^{(1)}$
$\lambda_2$	0.0933		-	-
$\lambda_3$	0		$\tau_{1/3}$	$\tau_{1/3}$
$\lambda_4$	-0.4128		$\mathbb{U}^+, \tau_{1/3}$	$\mathbb{U}^{(1)}, \tau_{1/3}$
$\lambda_{5,6}$	-0.6108	0.3759	$\mathbb{U}^+$	$\mathbb{U}^{(1)}$
$\lambda_{7,8}$	-0.6108	0.3759	-	-
$\lambda_9$	-1.6641		-	-
$\lambda_{10}$	-1.6641		$\mathbb{U}^+$	$\mathbb{U}^{(1)}$
<hr/>				
$TW_{\pm 1}$				
$\lambda_{1,2}$	0.1156	0.8173	-	-
$\lambda_{3,4}$	0.0337	0.4189	-	-
$\lambda_5$	0		-	-
$\lambda_6$	-0.2457		-	-
$\lambda_{7,8}$	-0.3213	0.9813	-	-
<hr/>				
$TW_{\pm 2}$				
$\lambda_1$	0.3370		-	-
$\lambda_2$	0		-	-
$\lambda_{3,4}$	-0.0096	0.6288	-	-
$\lambda_{5,6}$	-0.2619	0.5591	-	-
$\lambda_{7,8}$	-0.3067	0.0725	-	-

equilibria (2.15) with velocities  $c = \pm 0.73699$  and  $\pm 0.34954$  which we label  $TW_{\pm 1}$  and  $TW_{\pm 2}$ , for ‘traveling waves.’ The profiles of the two relative equilibria and their time evolution with eventual decay into the chaotic attractor are shown in Figure 5.3. The leading eigenvalues of  $TW_{\pm 1}$  and  $TW_{\pm 2}$  are listed in Table 5.1; those with  $\mu > -2.5$  are also plotted in Figure 5.2.

Table 5.2 lists equilibrium energy  $E$ , the local Poincaré section return time  $T$ , radially expanding Floquet multiplier  $\Lambda_e$ , and the least contracting Floquet multiplier  $\Lambda_c$  for all  $L = 22$  equilibria and relative equilibria. The return time  $T = 2\pi/\nu_e$  is given by the imaginary part of the leading complex eigenvalue, the expansion multiplier per one turn of the most unstable spiral-out by  $\Lambda_e \approx \exp(\mu_e T)$ , and the contraction rate along the slowest contracting stable eigendirection by  $\Lambda_c \approx \exp(\mu_c T)$ . We learn

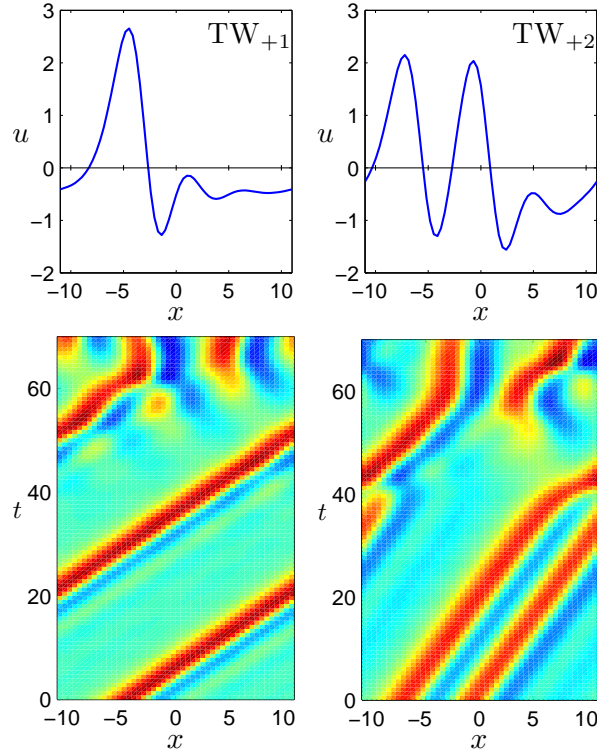


FIG. 5.3. Relative equilibria:  $TW_{+1}$  with velocity  $c = 0.737$  and  $TW_{+2}$  with velocity  $c = 0.350$ . The upper panels show the relative equilibria profiles. The lower panels show evolution of slightly perturbed relative equilibria and their decay into generic turbulence. Each relative equilibrium has a reflection symmetric partner related by  $u(x) \rightarrow -u(-x)$  travelling with velocity  $-c$ .

that the shortest ‘turn-over’ time is  $\approx 10 - 20$ , and that if there exist horseshoe sets of unstable periodic orbits associated with these equilibria, they have unstable multipliers of order of  $\Lambda_e \sim 5 - 10$ , and that they are surprisingly thin in the folding direction, with contracting multipliers of order of  $10^{-2}$ , as also observed in ref. [23].

TABLE 5.2

Properties of equilibria and relative equilibria determining the system dynamics in their vicinity.  $T$  is characteristic time scale of the dynamics,  $\Lambda_e$  and  $\Lambda_c$  are the leading expansion and contraction rates, and  $E$  is the energy (3.6).

	$E$	$T$	$\Lambda_e$	$\Lambda_c$
$E_1$	0.2609	18.81	4.79	0.04
$E_2$	0.4382	26.35	5.99	0.03
$E_3$	1.5876	10.71	9.92	0.01
$TW_{\pm 1}$	0.4649			
$TW_{\pm 2}$	0.6048			

**5.1. Unstable manifolds of equilibria and their heteroclinic connections.** As shown in Table 5.1, the  $E_1$  equilibrium has two unstable planes within which the solutions are spiralling out (that is, two pairs of complex conjugate eigenvalues). The  $E_2$  has one such plane, while the  $E_3$  has two real positive eigenvalues, so the solutions are moving radially away from the equilibrium within the plane spanned

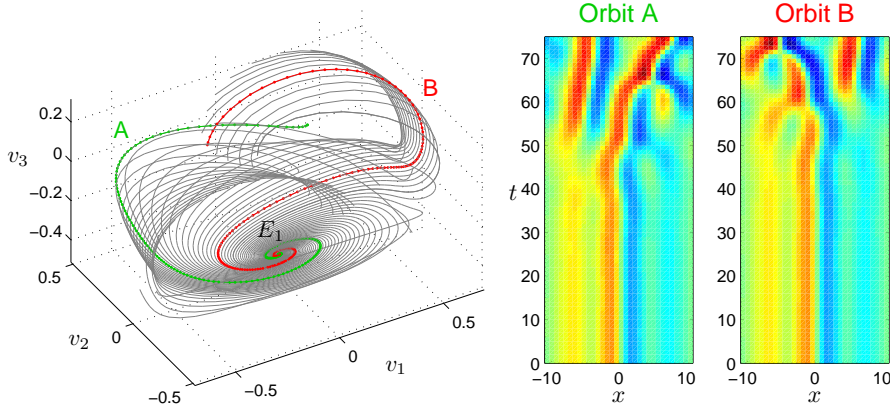


FIG. 5.4. The left panel shows the unstable manifold of equilibrium  $E_1$  starting within the plane corresponding to the first pair of unstable eigenvalues. The coordinate axes  $v_1$ ,  $v_2$ , and  $v_3$  are constructed from vectors  $\text{Re } \mathbf{e}^{(1)}$ ,  $\text{Im } \mathbf{e}^{(1)}$ , and  $\text{Re } \mathbf{e}^{(6)}$  by Gram-Schmidt orthogonalization. The right panel shows spatial representation of two orbits A and B. The change of color from blue to red indicates increasing values of  $u(x)$ .

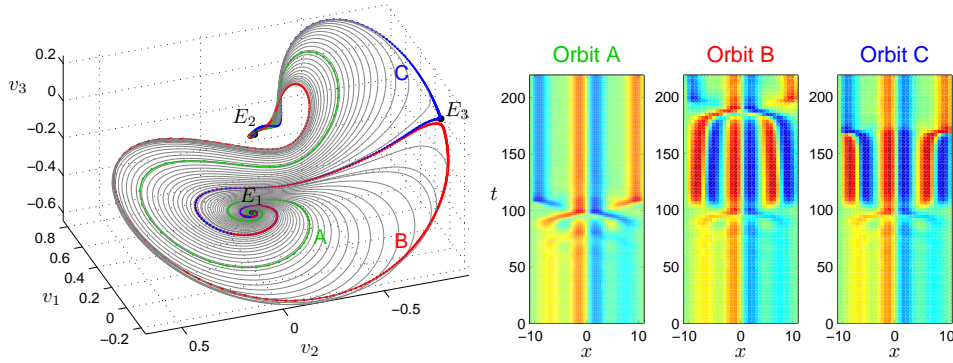


FIG. 5.5. The left panel shows the unstable manifold of equilibrium  $E_1$  starting within the plane corresponding to the second pair on unstable eigenvalues. The coordinate axes  $v_1$ ,  $v_2$ , and  $v_3$  are constructed from vectors  $\text{Re } \mathbf{e}^{(3)}$ ,  $\text{Im } \mathbf{e}^{(3)}$ , and  $\text{Re } \mathbf{e}^{(6)}$  by Gram-Schmidt orthogonalization. The right panel shows spatial representation of three orbits. Orbits B and C pass close to the equilibrium  $E_3$ .

by the corresponding eigenvectors. Since  $E_1$  has a larger unstable subspace, it is expected to have much less influence on the long time dynamics compared to  $E_2$  and  $E_3$ .

To construct an invariant manifold containing solutions corresponding to the pair of unstable complex conjugate eigenvalues,  $\lambda = \mu \pm i\nu$ ,  $\mu > 0$ , we start with a set of initial conditions near equilibrium  $E_k$ ,

$$a(0) = a_{E_k} + \epsilon \exp(\delta) \mathbf{e}^{(j)}, \quad (5.1)$$

where  $\delta$  takes the set of values uniformly distributed in the interval  $[0, 2\pi\mu/\nu]$ ,  $\mathbf{e}^{(j)}$  is a unit vector in the unstable plane, and  $\epsilon > 0$  is small.

The manifold starting within the first unstable plane of  $E_1$ , with eigenvalues  $0.1308 \pm i 0.3341$ , is shown in Figure 5.4. It appears to fall directly into the chaotic

attractor. The behavior of the manifold starting within the second unstable plane of  $E_1$ , eigenvalues  $0.0824 \pm i 0.3402$ , is remarkably different: as can be seen in Figure 5.5, almost all orbits within the manifold converge to the equilibrium  $E_2$ . The manifold also contains a heteroclinic connection from  $E_1$  to  $E_3$ , and is bordered by the  $\lambda_1$ -eigendirection unstable manifold of  $E_3$ .

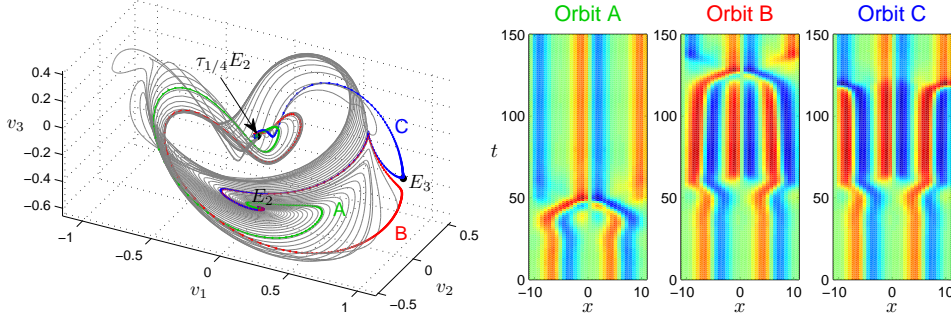


FIG. 5.6. The left panel shows the two-dimensional unstable manifold of equilibrium  $E_2$ . The coordinate axes  $v_1$ ,  $v_2$ , and  $v_3$  are constructed from vectors  $\text{Re } \mathbf{e}^{(1)}$ ,  $\text{Im } \mathbf{e}^{(1)}$ , and  $\mathbf{e}^{(7)}$  by Gram-Schmidt orthogonalization. The right panel shows spatial representation of three orbits. Orbits B and C pass close to the equilibrium  $E_3$ . See Figure 5.7 for a different visualization.

The two-dimensional unstable manifold of  $E_2$  is shown in Figure 5.6. All orbits within the manifold converge to  $E_2$  shifted by  $L/4$ . So this manifold can be viewed as a homoclinic connection. It also contains a pair of heteroclinic connections from  $E_2$  to  $E_3$ .

The equilibrium  $E_3$  has a pair of real unstable eigenvalues equal to each other. Therefore, within the plane spanned by the corresponding eigenvectors, the orbits move radially away from the equilibrium. In order to trace out the unstable manifold, we start with a set of initial conditions within the unstable plane

$$a(0) = a_{E_3} + \epsilon(v_1 \cos \phi + v_2 \sin \phi), \quad \phi \in [0, 2\pi], \quad (5.2)$$

where  $v_1$  and  $v_2$  are orthonormal vectors within the plane spanned by the two unstable eigenvectors, seeded as in (5.1). The unstable manifold of  $E_3$  is shown in Figure 5.8. The 3-fold symmetry of the manifold is related to the symmetry of  $E_3$  with respect to translation by  $L/3$ . The manifold contains heteroclinic orbits connecting  $E_3$  to three different points of the circle of equilibria  $E_2$  translated set of solutions. Note also that the segments of orbits B and C between  $E_3$  and  $E_2$  in Figures 5.5 and 5.6 represent the same heteroclinic connections as orbits B and C in Figure 5.8.

An understanding of the ubiquity of heteroclinic connections in KSe, as opposed to their non-genericity in a general high-dimensional system, is provided in ref. [20]. For our system size there are exactly two representatives of the  $E_2$  family that lie in the intersection of  $\mathbb{U}^+$  and  $\mathbb{U}^{(1)}$  related to each other by an  $L/4$  shift. Denote them by  $E_2$  and  $\tau_{1/4}E_2$  respectively. The unstable eigenplane of  $E_2$  lies on  $\mathbb{U}^+$  while that of  $\tau_{1/4}E_2$  lies on  $\mathbb{U}^{(1)}$ , cf. Table 5.1. The  $E_3$  family members that live in  $\mathbb{U}^+$  have one of their unstable eigenvectors (the one related to the heteroclinic connection to  $E_2$  family) on  $\mathbb{U}^+$ , while the other does not lie on symmetry-invariant subspace. Similarly, for the  $E_1$  family we observe that the equilibria in  $\mathbb{U}^+$  have an unstable plane on  $\mathbb{U}^+$  (again related to the heteroclinic connection) and a second one with no symmetry. Thus  $\tau_{1/4}E_2$  appears as a sink on  $\mathbb{U}^+$ , while all other equilibria appear



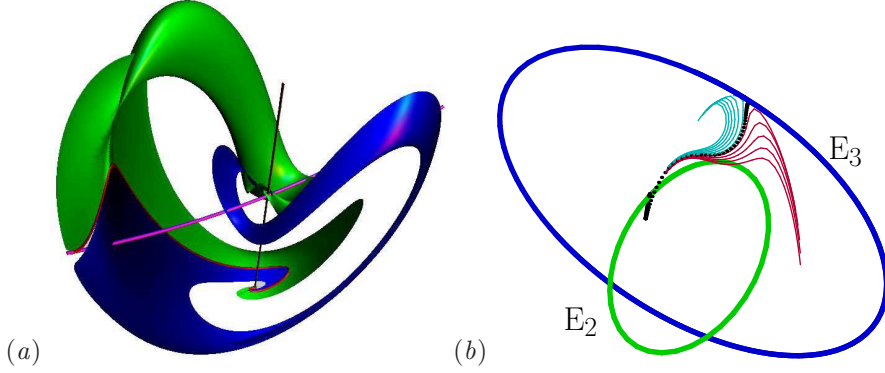


FIG. 5.7. (a) (blue/green) The unstable manifold of  $E_2$  equilibrium. (black line) The circle of  $E_2$  equilibria related by the translation invariance. (purple line) The circle of  $E_3$  equilibria. (red) The heteroclinic connection from the  $E_2$  equilibrium to the  $E_3$  equilibrium splits the manifold into two parts, colored (blue) and (green). See Figure 5.6 for a different visualization. (b)  $E_2$  equilibrium to  $E_3$  equilibrium heteroclinic connection. Here we omit the unstable manifold of  $E_2$ , keeping only a few neighboring trajectories in order to indicate the unstable manifold of  $E_3$ . The  $E_2$  and  $E_3$  families of equilibria arising from the continuous translational symmetry of KS on a periodic domain are indicated by the two circles.

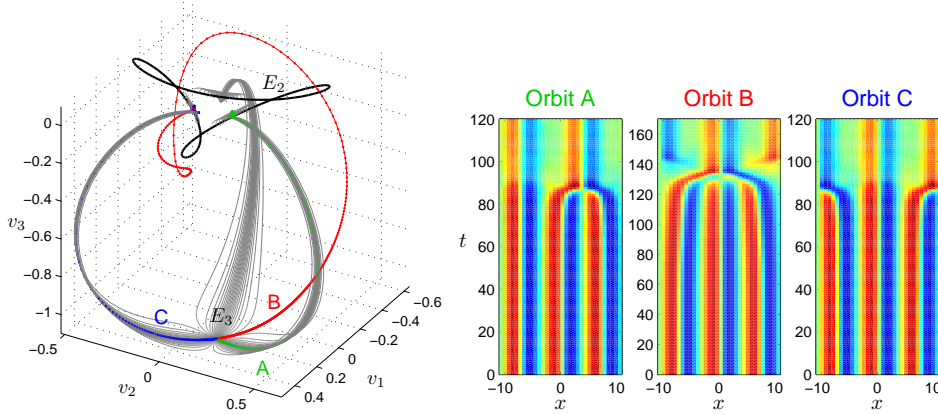



FIG. 5.8. The left panel shows the two-dimensional unstable manifold of equilibrium  $E_3$ . The coordinate axes  $v_1$ ,  $v_2$ , and  $v_3$  are constructed from vectors  $\mathbf{e}^{(1)}$ ,  $\mathbf{e}^{(2)}$ , and  $\mathbf{e}^{(4)}$  by Gram-Schmidt orthogonalization. The black line shows a family of  $E_2$  equilibria related by translational symmetry. The right panel shows spatial representation of three orbits. Orbits B and C are two different heteroclinic orbits connecting  $E_3$  to the same point on the  $E_2$  line.

as sources. This explains the heteroclinic connections from  $E_1$ ,  $E_2$  and  $E_3$  to  $\tau_{1/4}E_2$ . Observing that  $\tau_{1/4}\mathbb{U}^+ = \mathbb{U}^{(1)}$  and taking into account Table 5.1 we understand that within  $\mathbb{U}^{(1)}$  we have connections from  $\tau_{1/4}E_2$  (and members of  $E_1$  and  $E_3$  families) to  $E_2$  and the formation of a heteroclinic loop. Due to the translational invariance of KS there is a heteroclinic loop for any two points of the  $E_2$  family related by an  $L/4$ -shift. 

**6. Relative periodic orbits for  $L = 22$ .** The relative periodic orbits satisfy the condition (2.20)  $u(x + \ell_p, T_p) = u(x, 0)$ , where  $T_p$  is the period and  $\ell_p$  the phase shift. We have limited our search to orbits with  $T_p < 200$  and found over 300 relative

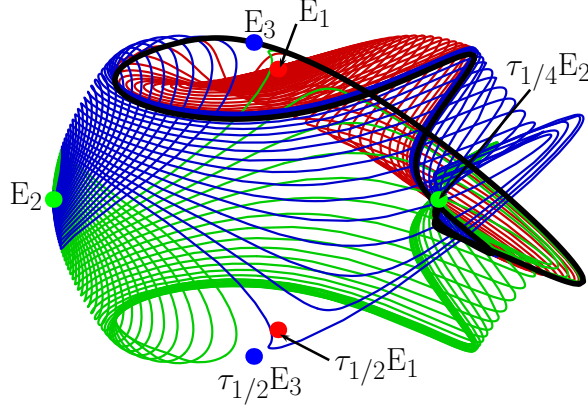


FIG. 5.9. Heteroclinic connections on  $\mathbb{U}^+$ : (red) The unstable manifold of  $E_1$  equilibrium. (blue/green) The unstable manifold of  $E_2$  equilibrium. (black) Heteroclinic connections from  $E_3$  equilibrium to  $\tau_{1/4}E_2$  equilibrium. The unstable manifolds of  $\tau_{1/2}E_1$  and  $\tau_{1/2}E_2$  have been omitted for clarity. Projection from 128 dimensions onto the plane given by the vectors  $E_2 - \tau_{1/4}E_2$  and  $E_3 - \tau_{1/2}E_3$ .

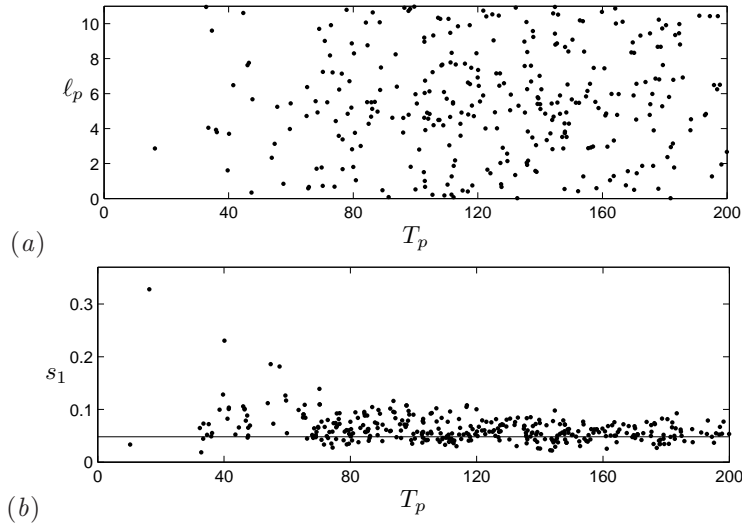


FIG. 6.1. (a) All relative periodic orbits of Kuramoto-Sivashinsky equation determined here, with periods  $T_p$  and shifts  $\ell_p > 0$ . (b) The largest Lyapunov exponents (6.1) of all relative periodic orbits and pre-periodic orbits with reflection. The horizontal line at 0.048 indicates the numerical value of the largest Lyapunov exponent of the chaotic attractor.

periodic orbits with  $\ell_p > 0$ . Each relative periodic orbit with phase shift  $\ell_p \neq 0$  has a reflection symmetric partner  $u_p(x) \rightarrow -u_p(-x)$  with phase shift  $-\ell_p$ .

The search has not been exhaustive, and there are likely to be more orbits with  $T_p < 200$ . However, the orbits we have found provide a representative sample of typical periodic and relative periodic orbits and approximate well the chaotic attractor (since they were located using seeds obtained from close returns within the chaotic dynamics).

Figure 6.1 (a) shows the relative periodic orbits in the plane  $(T, \ell)$ . Not much is

learned from such plot other than that for longer periods the relative periodic orbits are scattered over the whole  $(T, \ell)$  plane.

The stability of the orbits is determined by their Lyapunov exponents, defined as

$$s_j = \mu_j / T_p, \quad (6.1)$$

where  $\Lambda_j = e^{\mu_j \pm i\nu_j}$  are the eigenvalues of the fundamental matrix  $\mathbf{g}(\ell_p)J(a_p, T_p)$  (see Appendix B).

As was already the case for the Lyapunov exponents discussed in Sect. 4, for all periodic and relative periodic orbits we have found, only four Lyapunov exponents are dynamically relevant, with the remaining ones indicating strong contraction towards the 4-dimensional manifold containing the chaotic attractor. Out of the four leading exponents, two equal zero, due to the time and space translational invariance of the orbits. Of the remaining two, one is always positive, while the second one is either positive or negative.

The scatter of the largest Lyapunov exponents of periodic and relative periodic orbits is shown in Figure 6.1(b). In this case some tendency of accumulation toward the largest Lyapunov exponent 0.048 of the chaotic attractor can be noted. This, however, is in part an artifact of initializing the relative periodic orbit searches by near recurrences in long-time state space trajectories.

The small period relative periodic orbits outline the coarse structure of the chaotic attractor, while the longer period relative periodic orbits resolve the finer details of the dynamics. The first four orbits with the shortest periods we have found are shown in Figure 6.2(a-d). The shortest orbit with  $T_p = 16.4$  is also the most unstable, with one positive Lyapunov exponent equal 0.328. The other short orbits are less unstable, with the largest Lyapunov exponent in the range 0.018 – 0.073, typical of the long time attractor average.

We have found relative periodic orbits which stay close to the unstable manifold of  $E_2$ . As is illustrated in Figure 6.2(e-h), all such orbits have shift  $\ell_p \approx L/4$ , similar to the shift of orbits within the unstable manifold of  $E_2$ , which start at  $E_2$  and converge to  $\tau_{1/4}E_2$  (see Figure 5.6). This confirms that the ‘cage’ of unstable manifolds of equilibria plays an important role in organizing the chaotic dynamics of the Kuramoto-Sivashinsky equation.

**7. Pre-periodic orbits.** As discussed in Sect. 2.3, a relative periodic orbit will be periodic, that is,  $\ell_p = 0$ , if it either (a) lives within the  $\mathbb{U}^+$  antisymmetric subspace,  $-u(-x, 0) = u(x, 0)$ , or (b) returns to its reflection after a period:  $u(x, T_p) = -u(-x, 0)$ , and is thus periodic with period  $2T_p$ . The dynamics of Kuramoto-Sivashinsky equation in the antisymmetric subspace and periodic orbits with symmetry (a) have been investigated previously [3, 22, 23]. The KS equation with  $L = 22$  does not have any periodic orbits of this type.

We have found over 50 pre-periodic orbits with  $T_p < 100$  which possess the symmetry of type (b). Some of the shortest such orbits we have found are shown in Figure 6.2(i-l). Several were found as repeats of pre-periodic orbits during searches for relative periodic orbits with non-zero shifts, while most have been found as solutions of the pre-periodic orbit condition (2.21) with reflection, which takes form

$$-\mathbf{g}(-\ell)a^*(T_p) = a(0). \quad (7.1)$$

in the Fourier space representation (compare it to the condition (C.1) for relative periodic orbits).



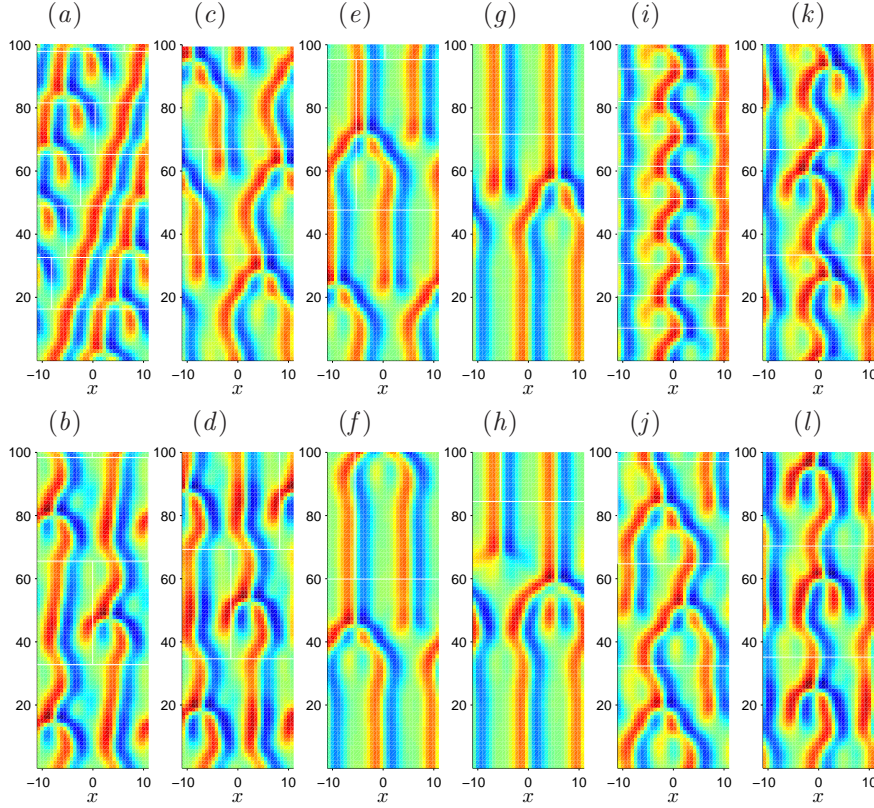


FIG. 6.2. Selected relative periodic and pre-periodic orbits of Kuramoto-Sivashinsky equation with  $L = 22$ : (a)  $T_p = 16.3$ ,  $\ell_p = 2.86$ ; (b)  $T_p = 32.8$ ,  $\ell_p = 10.96$ ; (c)  $T_p = 33.5$ ,  $\ell_p = 4.04$ ; (d)  $T_p = 34.6$ ,  $\ell_p = 9.60$ ; (e)  $T_p = 47.6$ ,  $\ell_p = 5.68$ ; (f)  $T_p = 59.9$ ,  $\ell_p = 5.44$ ; (g)  $T_p = 71.7$ ,  $\ell_p = 5.503$ ; (h)  $T_p = 84.4$ ,  $\ell_p = 5.513$ ; (i)  $T_p = 10.3$ ; (j)  $T_p = 32.4$ ; (k)  $T_p = 33.4$ ; (l)  $T_p = 35.2$ . Horizontal and vertical white lines indicate periodicity and phase shift of the orbits, respectively.

**8. Energy transfer rates.** In Figure 8.1 we plot (3.9), the time-dependent  $\dot{E}$  in the power input  $P$  vs. dissipation rate  $D$  plane, for  $L = 22$  equilibria and relative equilibria, a selected relative periodic orbit, and for a typical ‘turbulent’ long-time trajectory.

Projections from the  $\infty$ -dimensional state space onto the 3-dimensional  $(E, P, D)$  representation of the flow, such as Figures 8.1 and 8.2, can be misleading. The most one can say is that if points are clearly separated in an  $(E, P, D)$  plot (for example, in Figure 8.1  $E_1$  equilibrium is outside the recurrent set), they are also separated in the full state space. Converse is not true – states of very different topology can have similar energies.

An example is the relative periodic orbit  $(T_p, \ell_p) = (32.8, 10.96)$  (see Figure 6.2(b)) which appears well embedded within the turbulent flow. The mean power  $\overline{P_p}$  evaluated as in (3.11), see Figure 8.1, is numerically quite close to the long-time turbulent time average  $\overline{P}$ . Similarly close prediction of mean dissipation rate in the plane Couette flow from a single-period periodic orbit computed by Kawahara and Kida [19] has lead to optimistic hopes that ‘turbulence’ is different from low-dimensional chaos, insofar that the determination of one special periodic orbit could yield all long-time

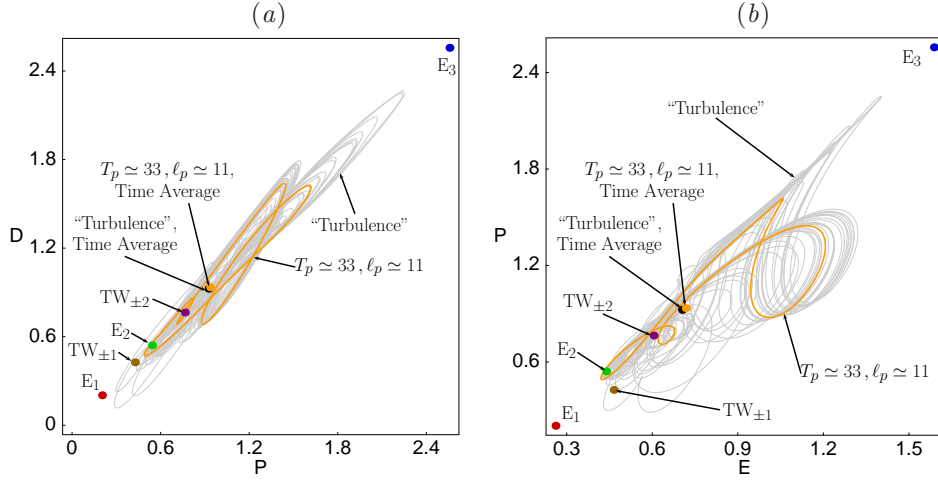


FIG. 8.1. (a) Power input  $P$  vs. dissipation rate  $D$  (b) energy  $E$  vs. power input  $P$ , for several equilibria and relative equilibria, a relative periodic orbit, and a typical ‘turbulent’ long-time trajectory. System size  $L = 22$ .

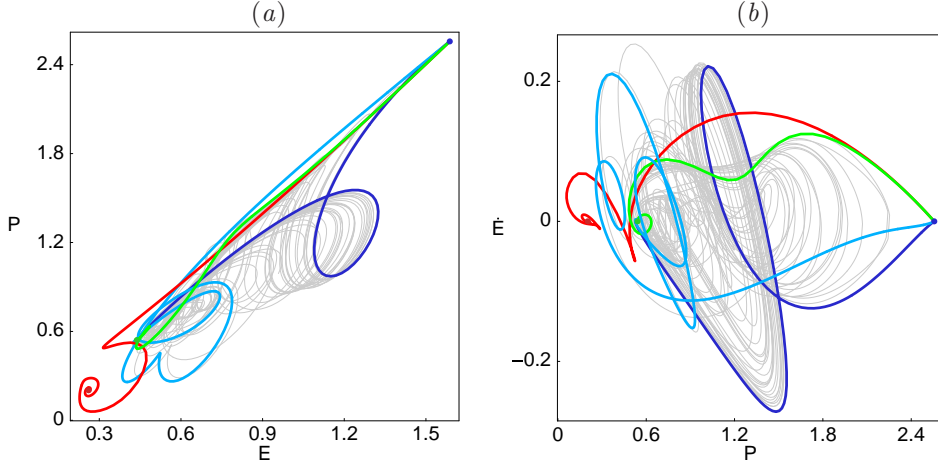


FIG. 8.2. Two projections of the  $(E, P, \dot{E})$  representation of the flow.  $E_1$  (red),  $E_2$  (green),  $E_3$  (blue), heteroclinic connections from  $E_2$  to  $E_3$  (green), from  $E_1$  to  $E_3$  (red) and from  $E_3$  to  $E_2$  (shades of blue), superimposed over a generic long-time ‘turbulent’ trajectory (grey). System size  $L = 22$ .

averages. Regrettably, not true – as always, here too one needs a hierarchy of periodic orbits of increasing length to obtain accurate predictions [7].

For any given relative periodic orbit a convenient visualization is offered by the *mean velocity frame*, that is, a reference frame that rotates with velocity  $v_p = \ell_p/T_p$ . In the mean velocity frame a relative periodic orbit becomes a periodic orbit, as in Figure 8.3 (b). However, each relative periodic orbit has its own mean velocity frame and thus sets of relative periodic orbits are difficult to visualize simultaneously.

**9. Summary.** In this paper we study the Kuramoto-Sivashinsky flow as a staging ground for testing dynamical systems approaches to moderate Reynolds number

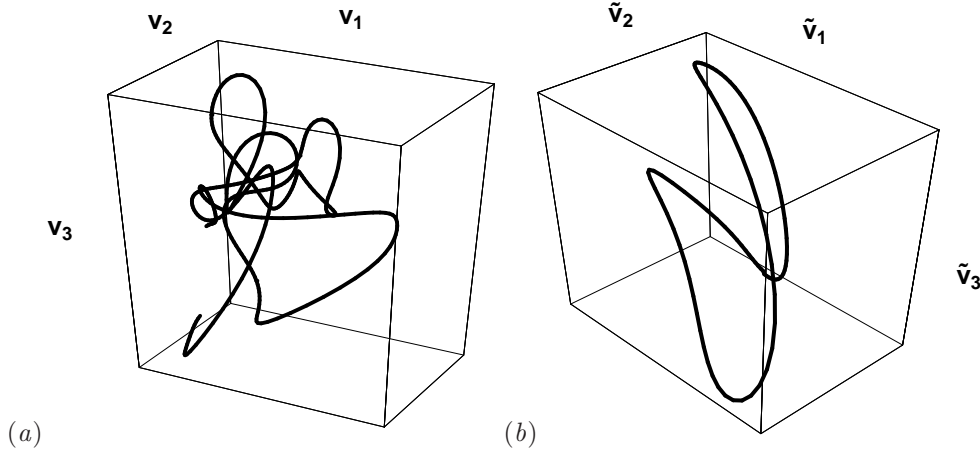


FIG. 8.3. The relative periodic orbit with  $(T_p, \ell_p) = (33.5, 4.04)$  from Figure 6.2(c) which appears well embedded within the turbulent flow: (a) A stationary state space projection, traced for four periods  $T_p$ . The coordinate axes  $v_1$ ,  $v_2$ , and  $v_3$  are those of Figure 5.6; (b) In the co-moving mean velocity frame, traced for one period  $T_p$ .

turbulence in full-fledged (*not* a few-modes model), infinite-dimensional state space PDE settings [16], and present a detailed geometrical portrait of dynamics in the Kuramoto-Sivashinsky state space for the  $L = 22$  system size, the smallest system size for which this system empirically exhibits “sustained turbulence”.

Compared to the earlier work [3, 22, 23, 24], the main advances here are the new insights in the role that continuous symmetries, discrete symmetries, low-dimensional unstable manifolds of equilibria, and the connections between equilibria play in organizing the flow. The key new feature of the translationally invariant KS on a periodic domain are the attendant continuous families of relative equilibria (traveling waves) and relative periodic orbits. We have now understood the preponderance of solutions of relative type, and lost fear of them: a large number of unstable relative periodic orbits and periodic orbits has been determined here numerically.

Visualization of infinite-dimensional state space flows, especially in presence of continuous symmetries, is not straightforward. At first glance, turbulent dynamics visualized in the state space appears hopelessly complex, but under a detailed examination it is much less so than feared: for strongly dissipative flows (KS, Navier-Stokes) it is pieced together from low dimensional local unstable manifolds connected by fast transient interludes. In this paper we offer two low-dimensional visualizations of such flows: (1) projections onto 2- or 3-dimensional, PDE representation independent dynamically invariant frames, and (2) projections onto the physical, symmetry invariant but time-dependent energy transfer rates.

Relative periodic orbits require a reformulation of the periodic orbit theory [6], as well as a rethinking of the dynamical systems approaches to constructing symbolic dynamics, outstanding problems that we hope to address in near future. What we have learned from the  $L = 22$  system is that many of these relative periodic orbits appear organized by the unstable manifold of  $E_2$ , closely following the homoclinic loop formed between  $E_2$  and  $\tau_{1/4}E_2$ .

The Kuramoto-Sivashinsky  $L = 22$  system size was chosen as the smallest system size for which KS empirically exhibits “sustained turbulence”. This is convenient both



for the analysis of the state space geometry, and for the numerical reasons, but the price is high - much of the observed dynamics is specific to this unphysical, externally imposed periodicity. What needs to be understood is the nature of equilibrium and relative periodic orbit solutions in the  $L \rightarrow \infty$  limit, and the structure of the  $L = \infty$  periodic orbit theory.

In summary, Kuramoto-Sivashinsky (and plane Couette flow, see ref. [13]) equilibria, relative equilibria, periodic orbits and relative periodic orbits embody Hopf's vision [17]: together they form the repertoire of recurrent spatio-temporal patterns explored by turbulent dynamics.

**Acknowledgments.** We are grateful to Y. Lan for pointing out to us the existence of the  $E_1$  equilibrium at the  $L = 22$  system size and J. Crofts for a key observation [5] that led to faster relative periodic orbit searches. R.L.D. gratefully acknowledges the support from EPSRC under grant GR/S98986/01.

### Appendix A. Integrating Kuramoto-Sivashinsky equation numerically.

The Kuramoto-Sivashinsky equation in terms of Fourier modes:

$$\hat{u}_k = \mathcal{F}[u]_k = \frac{1}{L} \int_0^L u(x, t) e^{-iq_k x} dx, \quad u(x, t) = \mathcal{F}^{-1}[\hat{u}] = \sum_{k \in \mathbb{Z}} \hat{u}_k e^{iq_k x} \quad (\text{A.1})$$

is given by

$$\dot{\hat{u}}_k = (q_k^2 - q_k^4) \hat{u}_k - \frac{iq_k}{2} \mathcal{F}[(\mathcal{F}^{-1}[\hat{u}])^2]_k. \quad (\text{A.2})$$

Since  $u$  is real, the Fourier modes are related by  $\hat{u}_{-k} = \hat{u}_k^*$ .

The above system is truncated as follows: The Fourier transform  $\mathcal{F}$  is replaced by its discrete equivalent

$$a_k = \mathcal{F}_N[u]_k = \sum_{n=0}^{N-1} u(x_n) e^{-iq_k x_n}, \quad u(x_n) = \mathcal{F}_N^{-1}[a]_n = \frac{1}{N} \sum_{k=0}^{N-1} a_k e^{iq_k x_n}, \quad (\text{A.3})$$

where  $x_n = 2\pi\tilde{L}/N$  and  $a_{N-k} = a_k^*$ . Since  $a_0 = 0$  due to Galilean invariance and setting  $a_{N/2} = 0$  (assuming  $N$  is even), the number of independent variables in the truncated system is  $N - 2$ :

$$\dot{a}_k = v_k(a) = (q_k^2 - q_k^4) a_k - \frac{iq_k}{2} \mathcal{F}_N[(\mathcal{F}_N^{-1}[a])^2]_k, \quad (\text{A.4})$$

where  $k = 1, \dots, N/2 - 1$ , although in the Fourier transform we need to use  $a_k$  over the full range of  $k$  values from 0 to  $N - 1$ . As  $a_k \in \mathbb{C}$ , (A.4) represents a system of ordinary differential equations in  $\mathbb{R}^{N-2}$ .

The discrete Fourier transform  $\mathcal{F}_N$  can be computed by FFT. In Fortran and C, the FFTW library ref. [10] can be used.

In order to find the Jacobian of the solution, or compute Lyapunov exponents of the Kuramoto-Sivashinsky equation, one needs to solve the equation for a displacement vector  $b$  in the tangent space:

$$\dot{b} = \frac{\partial v(a)}{\partial a} b. \quad (\text{A.5})$$



Since  $\mathcal{F}_N$  is a linear operator, it is easy to show that

$$\dot{b}_k = (q_k^2 - q_k^4) b_k - iq_k \mathcal{F}_N[\mathcal{F}_N^{-1}[a] \otimes \mathcal{F}_N^{-1}[b]]_k, \quad (\text{A.6})$$

where  $\otimes$  indicates componentwise product of two vectors, that is,  $a \otimes b = \text{diag}(a) b = \text{diag}(b) a$ . This equation needs to be solved simultaneously with (A.4).

Equations (A.4) and (A.6) were solved using the exponential time differencing 4th-order Runge-Kutta method (ETDRK4) [4, 18].

### Appendix B. Determining stability properties of equilibria, traveling waves, and relative periodic orbits.

Let  $f^t$  be the flow map of the Kuramoto-Sivashinsky equation, that is  $f^t(a) = a(t)$  is the solution of (A.4) with initial condition  $a(0) = a$ . The stability properties of the solution  $f^t(a)$  are determined by the fundamental matrix  $J(a, t)$  consisting of partial derivatives of  $f^t(a)$  with respect to  $a$ . Since  $a$  and  $f^t$  are complex valued vectors, the real valued matrix  $J(a, t)$  contains partial derivatives evaluated separately with respect to the real and imaginary parts of  $a$ , that is

$$J(a, t) = \frac{\partial f^t(a)}{\partial a} = \begin{pmatrix} \frac{\partial f_{R,1}^t}{\partial a_{R,1}} & \frac{\partial f_{R,1}^t}{\partial a_{I,1}} & \frac{\partial f_{R,1}^t}{\partial a_{R,2}} & & \\ \frac{\partial f_{I,1}^t}{\partial a_{R,1}} & \frac{\partial f_{I,1}^t}{\partial a_{I,1}} & \frac{\partial f_{I,1}^t}{\partial a_{R,2}} & \dots & \\ \frac{\partial f_{R,2}^t}{\partial a_{R,1}} & \frac{\partial f_{R,2}^t}{\partial a_{I,1}} & \frac{\partial f_{R,2}^t}{\partial a_{R,2}} & & \\ & \vdots & & \ddots & \end{pmatrix} \quad (\text{B.1})$$

where  $a_k = a_{R,k} + ia_{I,k}$  and  $f_k^t = f_{R,k}^t + if_{I,k}^t$ . The partial derivatives  $\frac{\partial f^t}{\partial a_{R,j}}$  and  $\frac{\partial f^t}{\partial a_{I,j}}$  are determined by solving (A.6) with initial conditions  $b_k(0) = b_{N-k}(0) = 1 + 0i$  and  $b_k(0) = -b_{N-k}(0) = 0 + 1i$ , respectively, for  $k = j$  and  $b_k(0) = 0$  otherwise.

The stability of a periodic orbit with period  $T_p$  is determined by the location of eigenvalues of  $J(a_p, T_p)$  with respect to the unit circle in the complex plane.

Because of the translation invariance, the stability of a relative periodic orbit is determined by the eigenvalues of the matrix  $\mathbf{g}(\ell_p) J(a_p, T_p)$ , where  $\mathbf{g}(\ell)$  is the action of the translation operator introduced in (2.6), which in real valued representation takes the form of a block diagonal matrix with the  $2 \times 2$  blocks

$$\begin{pmatrix} \cos q_k \ell & \sin q_k \ell \\ -\sin q_k \ell & \cos q_k \ell \end{pmatrix}, \quad k = 1, 2, \dots, N/2 - 1.$$

For an equilibrium solution  $a_q$ ,  $f^t(a_q) = a_q$  and so the fundamental matrix  $J(a_q, t)$  can be expressed in terms of the time independent stability matrix  $A(a_q)$  as follows

$$J(a_q, t) = e^{A(a_q)t},$$

where

$$A(a_q) = \left. \frac{\partial v}{\partial a} \right|_{a=a_q}. \quad (\text{B.2})$$

Using the real valued representation of (B.1), the partial derivatives of  $v(a)$  with respect to the real and imaginary parts of  $a$  are given by

$$\begin{aligned} \frac{\partial v_k}{\partial a_{R,j}} &= (q_k^2 - q_k^4) \delta_{kj} - iq_k \mathcal{F}_N[\mathcal{F}_N^{-1}[a] \otimes \mathcal{F}_N^{-1}[b_R^{(j)}]]_k, \\ \frac{\partial v_k}{\partial a_{I,j}} &= (q_k^2 - q_k^4) i \delta_{kj} - iq_k \mathcal{F}_N[\mathcal{F}_N^{-1}[a] \otimes \mathcal{F}_N^{-1}[b_I^{(j)}]]_k, \end{aligned} \quad (\text{B.3})$$

where  $b_R^{(j)}$  and  $b_I^{(j)}$  are complex valued vectors such that  $b_{R,k}^{(j)} = b_{R,N-k}^{(j)} = 1 + 0i$  and  $b_{I,k}^{(j)} = -b_{I,N-k}^{(j)} = 0 + 1i$  for  $k = j$  and  $b_{R,k}^{(j)} = b_{I,k}^{(j)} = 0$  otherwise. In terms of  $a_{R,k}$  and  $a_{I,k}$  we have

$$\begin{aligned}\frac{\partial v_{R,k}}{\partial a_{R,j}} &= (q_k^2 - q_k^4) \delta_{kj} + q_k (a_{I,k+j} + a_{I,k-j}), \\ \frac{\partial v_{R,k}}{\partial a_{I,j}} &= -q_k (a_{R,k+j} - a_{R,k-j}), \\ \frac{\partial v_{I,k}}{\partial a_{R,j}} &= -q_k (a_{R,k+j} + a_{R,k-j}), \\ \frac{\partial v_{I,k}}{\partial a_{I,j}} &= (q_k^2 - q_k^4) \delta_{kj} - q_k (a_{I,k+j} - a_{I,k-j}),\end{aligned}\tag{B.4}$$

where  $\delta_{kj}$  is Kronecker delta.

The stability of equilibria is characterized by the sign of the real part of the eigenvalues of  $A(a_q)$ . The stability of a relative equilibrium is determined in the co-moving reference frame, so the fundamental matrix takes the form  $\mathbf{g}(c_q t) J(a_q, t)$ . The stability matrix of a relative equilibrium is thus equal to  $A(a_q) + c_q \mathcal{L}$  where  $\mathcal{L} = iq_k \delta_{kj}$  is the Lie algebra translation generator, which in the real-space representation takes the form  $\mathcal{L} = \text{diag}(0, q_1, 0, q_2, \dots)$ .

### Appendix C. Levenberg–Marquardt searches for relative periodic orbits.

To find periodic and relative periodic orbits of the Kuramoto-Sivashinsky equation, we use multiple shooting and the Levenberg–Marquardt algorithm implemented in `lmdcr` from the MINPACK software package or function `fsolve` in Matlab.

Note that the LM algorithm is able to solve underdetermined systems of equations. Therefore, there is no need to augment the system with additional constraint equations, as is done in appendix D. For example, since López *et al.* [24] used `lmdcr` to find relative periodic orbits in CGLE, they did not need to augment their system with the three additional constraint equations. In fact, we have found that, with the additional constraint equations, the solver usually takes more steps to converge from the same seed, or fails to converge at all. Even though both `lmdcr` and `fsolve` solvers require that the number of variables does not exceed the number of equations, the additional equations can be set identically to zero [5].

We need to solve the system of  $N - 2$  equations

$$\mathbf{g}(\ell_p) f^{T_p}(a_p) - a_p = 0,\tag{C.1}$$

with  $N$  unknowns  $(a_p, T_p, \ell_p)$ , where  $f^t$  is the flow map of the Kuramoto-Sivashinsky equation.

We have tried two different implementations of the multiple shooting. The emphasis was on the simplicity of the implementations, so, even though both implementations worked equally well, each of them had its own minor drawbacks.

In the first implementation, we fix the total number of steps within each shooting stage and change the numerical integrator step size  $h$  in order to adjust the total integration time to a desired value  $T$ .

Let  $(a_0, T_0, \ell_0)$  be the starting guess for a relative periodic orbit obtained through a close return within a chaotic attractor. We require that the initial step does not

exceed  $h_0$ , so we round off the number of integration steps to  $n = \lceil T_0/h_0 \rceil$ , where  $\lceil x \rceil$  denotes the nearest integer larger than  $x$ .

The integration step size is equal to  $h = T/n$ . With the number of shooting stages equal to  $m$ , the system in (C.1) is rewritten as follows

$$\begin{aligned} F^{(1)} &= f^\tau(a^{(1)}) - a^{(2)} = 0, \\ F^{(2)} &= f^\tau(a^{(2)}) - a^{(3)} = 0, \\ &\dots \\ F^{(m-1)} &= f^\tau(a^{(m-1)}) - a^{(m)} = 0, \\ F^{(m)} &= \mathbf{g}(\ell) f^{\tau'}(a^{(m)}) - a^{(1)} = 0, \end{aligned} \tag{C.2}$$

where  $\tau = \lfloor n/m \rfloor h$  ( $\lfloor x \rfloor$  is the nearest integer smaller than  $x$ ),  $\tau' = nh - (m-1)\tau$ , and  $a^{(j)} = f^{(j-1)\tau}(a)$ ,  $j = 1, \dots, m$ . With the Jacobian of this system given by

$$J = \begin{pmatrix} \frac{\partial F^{(j)}}{\partial a^{(k)}} & \frac{\partial F^{(j)}}{\partial T} & \frac{\partial F^{(j)}}{\partial \ell} \end{pmatrix}, \quad j, k = 1, \dots, m, \tag{C.3}$$

the partial derivatives with respect to  $a^{(k)}$  can be calculated using the solution of (A.6) as described in Appendix B. The partial derivatives with respect to  $T$  are given by

$$\frac{\partial F^{(j)}}{\partial T} = \begin{cases} \frac{\partial f^\tau(a^{(j)})}{\partial \tau} \frac{\partial \tau}{\partial T} = v(f^\tau(a^{(j)})) \lfloor n/m \rfloor / n, & j = 1, \dots, m-1 \\ \mathbf{g}(\ell) v(f^{\tau'}(a^{(j)})) (1 - \frac{m-1}{n} \lfloor n/m \rfloor), & j = m. \end{cases} \tag{C.4}$$

Note that, even though  $\partial f^t(a)/\partial t = v(f^t(a))$ , it should not be evaluated using equation for the vector field. The reason is that, since the flow  $f^t$  is approximated by a numerical solution, the derivative of the numerical solution with respect to the step size  $h$  may differ from the vector field  $v$ , especially for larger step sizes. We evaluate the derivative by a forward difference using numerical integration with step sizes  $h$  and  $h + \delta$ :

$$\frac{\partial f^{jh}(a)}{\partial t} = \frac{1}{j\delta} \left[ f^{j(h+\delta)}(a) - f^{jh}(a) \right], \quad j \in \mathbb{Z}^+ \tag{C.5}$$

with  $t = jh$  and  $\delta = 10^{-7}$  for double precision calculations. Partial derivatives  $\partial F^{(j)}/\partial \ell$  are all equal to zero except for  $j = m$ , where it is given by

$$\frac{\partial F^{(m)}}{\partial \ell} = \frac{d\mathbf{g}}{d\ell} f^{\tau'}(a^{(m)}). \tag{C.6}$$

This Jacobian is supplied to the routine `lmdcr` or `fsolve` augmented with two rows of zeros corresponding to the two identical zeros augmenting (C.3) in order to make the number of equations formally equal to the number of variables, as discussed above.

In the second implementation, we keep  $h$  and  $\tau$  fixed and vary only  $\tau' = T - (m-1)\tau$ . In this case, we need to be able to determine the numerical solution of Kuramoto-Sivashinsky equation not only at times  $t_j = jh$ ,  $j = 1, 2, \dots$ , but at any intermediate time as well. We do this by a cubic polynomial interpolation through points  $f^{t_j}(a)$  and  $f^{t_{j+1}}(a)$  with slopes  $v(f^{t_j}(a))$  and  $v(f^{t_{j+1}}(a))$ . The difference from the first

implementation is in that partial derivatives  $\partial F^{(j)}/\partial T$  are zero for all  $j = 1, \dots, m-1$ , except for

$$\frac{\partial F^{(m)}}{\partial T} = \mathbf{g}(\ell)v(f^{\tau'}(a^{(m)})). \quad (\text{C.7})$$

which, for consistency, needs to be evaluated from the cubic polynomial, not from the flow equation evaluated at  $f^{\tau'}(a^{(m)})$ .

We found the second implementation more convenient.

For detecting periodic and relative periodic orbits of the Kuramoto-Sivashinsky equation with  $L = 22$ , we used  $N = 32$ ,  $h = 0.25$  (or  $h_0 = 0.25$  within the first implementation), and the number of shooting stages such that  $\tau \approx 6.0$ . Once a relative periodic orbit is found, its existence in the Kuramoto-Sivashinsky PDE is verified numerical approximation improved by increasing the number of Fourier modes ( $N = 64$ ) and reducing the step size ( $h = 0.1$ ).

#### Appendix D. Newton method for relative periodic orbit searches.

Alternatively one can use Newton's shooting method with auxiliary conditions as in ref. [29].

Let  $a$ ,  $T$  and  $\ell$  be our guess cycle point, period, and shift, respectively. Taylor expand  $\mathbf{g}(\ell_p)f^{T_p}(a_p)$  in (C.1) around  $(a, T, \ell)$  to linear order in  $(\delta a, \delta T, \delta \ell) = (a_p - a, T_p - T, \ell_p - \ell)$ :

$$(1 - \mathbf{g}(\ell)J(a, T))\delta a - \mathbf{g}(\ell)v(f^T(a))\delta T - \mathcal{L}\mathbf{g}(\ell)f^T(a)\delta \ell \simeq \mathbf{g}(\ell)f^T(a) - a, \quad (\text{D.1})$$

where  $\mathcal{L}_{kj} = iq_k\delta_{kj}$  is the Lie algebra translation generator. The matrix  $\mathbf{g}(\ell)J(a, T)$  has two unit eigenvalues on the relative periodic orbit  $p$ , one associated with the invariance along the direction of the flow and the other with the translational invariance of the system. Thus (D.1) needs to be augmented by two conditions to eliminate the (close to) zero eigenvalues of  $1 - \mathbf{g}(\ell)J(a, T)$ . Following ref. [29] we impose dropped: locally transverse sections conditions

$$v(a) \cdot \delta a = 0, \quad (\mathcal{L}\mathbf{g}a) \cdot \delta a = 0. \quad (\text{D.2})$$

The requirement imposed by (D.2) on the variations of the initial  $\delta a$  of (D.1) is that they vanish along the directions of the flow and of infinitesimal translations.

#### REFERENCES

- [1] J. C. BRONSKI AND T. N. GAMBILL, *Uncertainty estimates and  $L_2$  bounds for the Kuramoto-Sivashinsky equation*, 2006, arXiv:math/0508481.
- [2] A. CHENCINER, [www.imcce.fr/Equipes/ASD/person/chenciner/chenciner.html](http://www.imcce.fr/Equipes/ASD/person/chenciner/chenciner.html).
- [3] F. CHRISTIANSEN, P. CVITANOVIĆ, AND V. PUTKARADZE, *Spatiotemporal chaos in terms of unstable recurrent patterns*, Nonlinearity, 10 (1997), p. 55.
- [4] S. M. COX AND P. C. MATTHEWS, *Exponential time differencing for stiff systems*, J. Comp. Phys., 176 (2002), pp. 430–455.
- [5] J. J. CROFTS, *Efficient method for detection of periodic orbits in chaotic maps and flows*, PhD thesis, University of Leicester, Leicester, UK, April 2007, arXiv:nlin.CD/0706.1940.
- [6] P. CVITANOVIĆ, *Continuous symmetry reduced trace formulas*. [ChaosBook.org/predrag/papers/trace.pdf](http://ChaosBook.org/predrag/papers/trace.pdf), 2007.
- [7] P. CVITANOVIĆ, R. ARTUSO, R. MAINIERI, G. TANNER, AND G. VATTAY, *Chaos: Classical and Quantum*, Niels Bohr Institute, Copenhagen, 2005, ChaosBook.org.
- [8] P. CVITANOVIĆ AND B. ECKHARDT, *Symmetry decomposition of chaotic dynamics*, Nonlinearity, 6 (1993), p. 277, arXiv:chao-dyn/9303016.

- [9] C. FOIAS, B. NICOLAENKO, G. R. SELL, AND R. TEMAM, *Inertial manifold for the Kuramoto-Sivashinsky equation*, C. R. Acad. Sci. I-Math, 301 (1985), pp. 285–288.
- [10] M. FRIGO AND S. G. JOHNSON, *The design and implementation of FFTW3*, Proceedings of the IEEE, 93 (2005), pp. 216–231. special issue on "Program Generation, Optimization, and Platform Adaptation".
- [11] U. FRISCH, Z. S. SHE, AND O. THUAL, *Viscoelastic behavior of cellular solutions to the Kuramoto-Sivashinsky model*, J. Fluid Mech., 168 (1986), pp. 221–240.
- [12] L. GIACOMELLI AND F. OTTO, *New bounds for the Kuramoto-Sivashinsky equation*, Comm. Pure Appl. Math., 58 (2005), pp. 297–318.
- [13] J. F. GIBSON, J. HALCROW, AND P. CVITANOVIĆ, *Visualizing the geometry of state-space in plane Couette flow*. submitted to J. Fluid Mech., 2007, arXiv:0705.3957.
- [14] J. M. GREENE AND J. S. KIM, *The steady states of the Kuramoto-Sivashinsky equation*, Physica D, 33 (1988), pp. 99–120.
- [15] B. HOF, C. W. H. VAN DOORNE, J. WESTERWEEL, F. T. M. NIEUWSTADT, H. FAISST, B. ECKHARDT, H. WEDIN, R. R. KERSWELL, AND F. WALEFFE, *Experimental observation of nonlinear traveling waves in turbulent pipe flow*, Science, 305 (2004), pp. 1594–1598, <http://www.sciencemag.org/cgi/reprint/305/5690/1594.pdf>.
- [16] P. HOLMES, J. L. LUMLEY, AND G. BERKOOZ, *Turbulence, Coherent Structures, Dynamical Systems and Symmetry*, Cambridge University Press, Cambridge, 1996.
- [17] E. HOPF, *A mathematical example displaying features of turbulence*, Comm. Appl. Math., 1 (1948), pp. 303–322.
- [18] A.-K. KASSAM AND L. N. TREFETHEN, *Fourth-order time stepping for stiff PDEs*, SIAM J. Sci. Comput., 26 (2005), pp. 1214–1233.
- [19] G. KAWAHARA AND S. KIDA, *Periodic motion embedded in plane Couette turbulence: regeneration cycle and burst*, J. Fluid Mech., 449 (2001), pp. 291–300.
- [20] I. G. KEVREKIDIS, B. NICOLAENKO, AND J. C. SCOVEL, *Back in the saddle again: a computer assisted study of the Kuramoto-Sivashinsky equation*, SIAM J. Appl. Math., 50 (1990), pp. 760–790.
- [21] Y. KURAMOTO AND T. TSUZUKI, *Persistent propagation of concentration waves in dissipative media far from thermal equilibrium*, Progr. Theor. Phys., 55 (1976), p. 365.
- [22] Y. LAN, *Dynamical systems approach to 1-d spatiotemporal chaos – A cyclist’s view*, PhD thesis, School of Physics, Georgia Institute of Technology, Atlanta, 2004.
- [23] Y. LAN AND P. CVITANOVIĆ, *Unstable recurrent patterns in Kuramoto-Sivashinsky dynamics*. In preparation, 2007.
- [24] V. LÓPEZ, P. BOYLAND, M. T. HEATH, AND R. D. MOSER, *Relative periodic solutions of the Complex Ginzburg-Landau equation*, SIAM J. Appl. Dyn. Syst., 4 (2005), p. 1042.
- [25] D. MICHELSON, *Steady solutions of the Kuramoto-Sivashinsky equation*, Physica D, 19 (1986), pp. 89–111.
- [26] R. E. L. QUEY, S. M. MAHAJAN, P. H. RUTHERFORD, AND W. M. TANG, *Nonlinear saturation of the trapped-ion mode*, Phys. Rev. Lett., 34 (1974), pp. 391–394.
- [27] G. I. SIVASHINSKY, *Nonlinear analysis of hydrodynamical instability in laminar flames - I. Derivation of basic equations*, Acta Astr., 4 (1977), p. 1177.
- [28] V. SZEBEHELY, *Theory of orbits*, Academic Press, New York, 1967.
- [29] D. VISWANATH, *Recurrent motions within plane Couette turbulence*, J. Fluid Mech., 580 (2007), pp. 339–358, arXiv:physics/0604062.